



On the Origin of Reversible and Irreversible Reactions in $\text{LiNi}_x\text{Co}_{(1-x)/2}\text{Mn}_{(1-x)/2}\text{O}_2$

Karin Kleiner,^{1,*,z} Claire A. Murray,² Cristina Grosu,^{3,4} Bixian Ying,¹ Martin Winter,^{1,5,*} Peter Nagel,⁶ Stefan Schuppler,⁶ and Michael Merz^{6,=}

¹Münster Electrochemical Energy Technology (MEET), University of Münster (WWU), 48149 Münster, Germany

²Beamline I11, Diamond Light Source (I11, DLS), Harwell Science and Innovation Campus, Diamond House, Didcot OX11 0DE, United Kingdom

³Institute of Energy and Climate Research, Research Center Jülich (IEK9, FZJ), 52425 Jülich, Germany

⁴Chair of Theoretical Chemistry, Technical University of Munich (TUM), 85747 Garching, Germany

⁵Helmholtz-Institute Münster, Forschungszentrum Jülich GmbH, 48149 Münster, Germany

⁶Institute for Quantum Materials and Technologies, Karlsruhe Institute of Technology (IQMT, KIT), 76344 Eggenstein-Leopoldshafen, Germany

Bond formation and breakage is crucial upon energy storage in lithium transition metal oxides (LiMeO_2 , $\text{Me} = \text{Ni, Co, Mn}$), i.e., the conventional cathode materials in Li ion batteries. Near-edge X-ray absorption finestructure spectroscopy (NEXAFS) of the Me L and O K edge performed upon the first discharge of $\text{LiNi}_x\text{Co}_{(1-x)/2}\text{Mn}_{(1-x)/2}\text{O}_2$ ($x = 0.33$: NCM111, $x = 0.6$: NCM622, $x = 0.8$: NCM811) in combination with charge transfer multiplet (CTM) calculations provide unambiguous evidence that redox reactions in NCMs proceed via a reversible oxidation of Ni associated with the formation of covalent bonds to O neighbors, and not, as widely assumed, via pure cationic or more recently discussed, pure anionic redox processes. Correlating these electronic changes with crystallographic data using *operando* synchrotron X-ray powder diffraction (XRPD) shows that the amount of ionic Ni limits the reversible capacity— at states of charge where all ionic Ni is oxidized (above 155 mAh g^{-1}), the lattice parameters collapse, and irreversible reactions are observed. Yet the covalence of the Ni–O bonds also triggers the electronic structure and thus the operation potential of the cathodes.

© 2021 The Author(s). Published on behalf of The Electrochemical Society by IOP Publishing Limited. This is an open access article distributed under the terms of the Creative Commons Attribution Non-Commercial No Derivatives 4.0 License (CC BY-NC-ND, <http://creativecommons.org/licenses/by-nc-nd/4.0/>), which permits non-commercial reuse, distribution, and reproduction in any medium, provided the original work is not changed in any way and is properly cited. For permission for commercial reuse, please email: permissions@iopublishing.org. [DOI: 10.1149/1945-7111/ac3c21]



Manuscript submitted August 31, 2021; revised manuscript received October 26, 2021. Published December 20, 2021.

Reaching global emission targets requires a widespread adoption of environmentally sustainable electric vehicles since the heavy reliance of the transport industry on fossil fuels means it is currently producing more than 30% of all greenhouse gas emissions.^{1,2} Li ion battery driven vehicles offer a Well-to-Wheel efficiency of up to 70% with the possibility of zero greenhouse gas emissions upon driving if the electricity is supplied by renewable energy sources.³ Thus electric vehicles (EVs) cannot only mitigate pollution issues from traffic, in fact greenhouse gas emissions can exclusively be generated in the manufacturing and recycling process which allows for large-scale treatment to further reduce the CO₂ footprint of the technology.⁴ Although electric vehicles which use Li ion batteries as power supply have reached market maturity,^{5,6} even higher energy densities (capacity × discharge voltage) and longer lifetimes are required for a widespread adoption and a use for heavy traffic. The limiting component in current generations of Li-ion batteries is the cathode material.^{7–10}

The most commercially used and promising future cathode materials belong to the class of rhombohedral, layered oxides (LiMeO_2 , $\text{Me} = \text{Ni, Co, Mn, Li, Al, Mg}$) or structurally related materials.^{7–11} A large number of these materials exist and Ni- and Li-rich layered oxides show the highest energy densities.^{7,12} Cathode materials undergo reversible electron exchange (redox) reactions when they release and accommodate Li ions upon charge and discharge. This is challenging from a materials perspective due to the associated large crystallographic and electronic changes that lead to a limitation in energy density and to severe degradation reactions, in particular for Ni containing layered oxides.^{13–15} While changes in the crystallographic structure are relatively easy to monitor and are consequently well understood,^{13,16–22} the investigation of electronic properties and changes remains more challenging due to the need of either soft X-ray absorption or emission spectroscopy, for which the

techniques require ultra-high vacuum^{23–29} but also a complex many body approach (ab initio calculations based on DFT) to understand the electronic structure (the core level spectra) of the materials.^{30–36} The advantage of soft X-rays (excitation energies < 1000 eV) over hard X-rays (excitation energies > 1000 eV) for the analysis of transition metal oxides originates from dipole selection rules: The transition matrix element is non-zero only if the change in angular momentum Δl is ± 1 . Thus, electron excitations from the Me L edge into Me 3d and from the O K edge into O 2p valence states are dipole allowed (energy requirements: 500 eV–1000 eV) while this is not the case for excitations from the Me K edge into $3d$ orbitals (energy requirements > 1000 eV).

Tarascon et al. showed early on that the charge compensation in Li_xMeO_2 ($0.56 \leq x \leq 1$) is much more complex than the widely accepted cationic redox process ($\text{Me}^{2+ \text{ or } 3+} \rightleftharpoons \text{Me}^{4+} + 1 \text{ or } 2 \text{ e}^-$) indicates.³⁷ Based on changes in the Me-O distance upon charge and discharge this work suggests that the reversible process includes hybridizations of Me 3d and O 2p states (covalence) and thus shows that lattice O contributes to the charge compensation. Many more publications followed on this approach with a focus on the anionic oxidation/reduction of O in Li/Na-rich layered oxides,^{38–44} a redox mechanism which is even more complex if compared to NCMs.⁴⁵

The present work revisits the intriguing question about the reversible redox process in NCMs and the covalence of Me-O bonds while putting emphasis on its importance in understanding capacity and voltage limitations. It also complements more recent studies claiming that oxygen is reversibly oxidized/reduced upon charge and discharge ($\text{O}^{2-} \rightleftharpoons \text{O}^{(2-x)-} + x \text{ e}^-$, $0 < x < 1$, so-called “anionic redox”) in NCMs, especially at high states of charge.^{46–48} The capacity and the open cell voltage are determined by the valence states of the redox active centers^{49–51} which are investigated with near edge X-ray absorption fine structure spectroscopy (NEXAFS) at the transition metal (Me) $L_{2,3}$ and oxygen (O) K edges in combination with charge transfer multiplet (CTM) calculations. The results provide unique insights into oxidation and reduction processes in Ni containing layered oxides and enables the study of changes in the

⁼These authors contributed equally to this work.

*Electrochemical Society Fellow.

^zE-mail: karin.kleiner@wwu.de

electronic nature of *Me*-O states (e.g., the ligand character of *Me* 3d states and thus the covalence of *Me*-O bonds). The results suggest that the redox processes at *Me* sites are always affiliated with a change in *Me*-O hybridization, ruling out that pure cationic or anionic redox processes occur at any point upon cycling. The combination of the NEXAFS results with *operando* synchrotron powder diffraction (SXPd) further enables the exploration of stability limits of the cathodes.

Experimental

Synthesis and electrode preparation.—LiNi_{1/3}Co_{1/3}Mn_{1/3}O₂ (NCM111), LiNi_{0.6}Co_{0.2}Mn_{0.2}O₂ (NCM622) and LiNi_{0.8}Co_{0.1}Mn_{0.1}O₂ (NCM811) were synthesized using a co-precipitation method in a continuous stirred tank reactor as described in Refs. 52, 53. LiNiO₂ (LNO) and LiCoO₂ (LCO) were synthesized using a sol-gel approach⁵⁴ and Li₂MnO₃ (LLO) was synthesized via a solid-state route.⁵⁵ Electrode preparation was performed using 92.5 wt-% of the cathode material (powder), 4 wt-% Imerys Super C65, 3.5 wt-% PvdF (Solef, Polyvinylidene difluoride, PvdF) and NMP (N-methylpyrrolidone) as processing solvent (6.5 mg). The ink was casted on an Al-foil (250 μm wet film thickness) and dried at 80 °C. 11 mm in diameter samples were punched out of the electrodes, pressed to achieve a tab density of ~30%, again dried in a Büchi oven (120 °C, 10⁻³ mbar, air free transfer into the glovebox) and assembled to a battery cell in an argon filled glovebox using Swagelok cells with two glass-fiber separators (11 mm in diameter, glass micro fiber 691, VWR, Germany), 60 μl LP57 (1 M LiPF₆ in ethylene carbonate (EC):ethyl methyl carbonate (EMC), 3:7 by weight, <20 ppm of H₂O, BASF SE, Germany) and lithium foil as counter electrodes (11 mm in diameter, 99.9% Rockwood Lithium, United States). The underlying capacity used to calculate the C-rate for NCM111, NCM622, NCM811, LNO, LCO and LLO was 160 mAh g⁻¹, 175 mAh g⁻¹, 180 mAh g⁻¹, 180 mAh g⁻¹, 140 mAh g⁻¹, 250 mAh g⁻¹, respectively. The applied voltage cut-offs upon galvanostatic cycling were chosen to be 4.3 V and 3.0 V.

Sample preparation for NEXAFS spectroscopy.—For NEXAFS sample preparation different electrodes were cycled with C/20 at 25 °C to the charged state, to a remaining capacity of 150 mAh g⁻¹, 100 mAh g⁻¹ and 50 mAh g⁻¹ in the first discharge and to the discharged state. After cycling, the cells were disassembled in an argon filled glovebox. Additional NCM111 samples cycled for 100 cycles were measured after disassembly, rinsed with dimethyl carbonate (DMC, BASF SE, Germany) and measured again in order to probe the impact of electrolyte decomposition products on the fluorescence yield NEXAFS spectra (Appendix A). All samples were dried in a Büchi oven (10⁻³ mbar, 25 °C) prior to the measurements without contact to air to avoid outgassing in the UHV chamber. An argon filled transfer case was used for the sample transfer from the glovebox to the load lock of the beamline since NCMs (especially in their charged state) are air sensitive.

NEXAFS.—NEXAFS measurements were performed at IQMT's soft X-ray beamline WERA at the Karlsruhe synchrotron light source KARA (Germany). NEXAFS measurements at the Ni L_{2,3}, Co L_{2,3}, Mn L_{2,3}, O K and F K edge were carried out in fluorescence yield (FY) detection mode. For the Co L_{2,3} edge measurements, the FY detection window (width 0.24 keV) was shifted up in energy from its nominal center position to minimize crosstalk of the signal from the preceding F K edge (see discussion in Appendix A). In the case of the Mn L_{2,3} edge, inverse partial FY detection (IPFY)⁵⁵ using the O K fluorescence was employed. The photon-energy resolution in the spectra was set to 0.2–0.4 eV. Energy calibration (using a NiO reference), dark current subtraction, division by I₀, background subtraction, data normalization and absorption correction was performed as described in Refs. 56, 57. The background treatment of the Ni L_{2,3} and Co L_{2,3} edges was more challenging due to the presence of F K EXAFS features and a detailed description is given

in Appendix A. Data evaluation of the *Me* L_{2,3} edges was done using charge-transfer multiplet calculations (CTM4XAS, Crispy and Quanty^{30–33}). The calculated spectra were fitted to the measured data with our Excel macro, applying a least squares method to minimize the difference in area between the data and the fit by shifting the calculated spectra along the energy axis and varying the intensity.

Synchrotron X-ray powder diffraction.—Time-resolved *operando* synchrotron X-ray powder diffraction (SXPd) of the first discharge (and after 50 cycles at 45 °C) was performed at beamline I11 (Diamond Light Source, UK) using the position sensitive detector (PSD) of the beamline.⁵⁸ The energy of the X-ray beam was tuned to 25 keV and the calibrated wavelength was 0.489951 (10) Å. The battery cells were mounted on a xyz-stage and each cell was adjusted to the center of diffraction. The 2D data was refined using the software package Fullprof (2θ range: 5°–65°).⁵⁹ Due to preferential orientations of Al (current collector of the NCM electrode) and Li (counter electrode), the phases were included in the refinements using the Le Bail method. The structural input parameters for the refinements of NCM111, NCM622 and NCM811 (in the pristine state) were obtained from crystallographic data files.^{60–62} Upon charge anisotropic micro-strain is increasing, which was implemented as described in Ref. 16.

Results

NCM811 (LiNi_{0.8}Co_{0.1}Mn_{0.1}O₂) and NCM622 (LiNi_{0.6}Co_{0.2}Mn_{0.2}O₂) show a 20 mAh g⁻¹–25 mAh g⁻¹ higher capacity than NCM111 (LiNi_{0.33}Co_{0.33}Mn_{0.33}O₂), Fig. 1A. The rate capability of the layered oxides, however, is remarkably similar although NCM811 suffers from a faster capacity decay at high cycling rates (after 25 cycles) if compared to NCM111 and NCM622. More information on the characteristics and the long term performance of the NCMs is provided in Appendix B and C. The dq/dV plots of the first cycle, for which the peaks can be assigned to reduction and oxidation processes, are given in Fig. 1B. Reference dq/dV plots of LiNiO₂ (LNO), LiCoO₂ (LCO) and Li₂MnO₃ (LLO) (dashed lines in Fig. 1B) reveal that redox reactions observed in NCMs occur at similar voltages as it is the case for LNO. The dq/dV peaks in LCO appear at significantly higher voltages while LLO does not show any significant redox activity between 3.0V and 4.3 V, the operation voltage of NCMs. The choice of the reference material is discussed in Appendix D. NEXAFS spectra were taken upon the first discharge of the materials (Fig. 1C, blue circles 1–5). The spectra are shown in Figs. 1D–1F (Ni L_{2,3} and O K edges, also labelled with blue circles 1–5) and Appendix C (Mn L_{2,3} and Co L_{2,3} edges).

NEXAFS is a powerful technique to study the electronic structure of materials if analyzed on edges allowing core electrons to be excited into valence states (3d and O 2p orbitals in case of NCMs) following dipole selection rules.^{27,30} Allowed transitions of the 1st order do correspond to the type *Me* 2p⁶ 3dⁿ → *Me* 2p⁵ 3dⁿ⁺¹ (*Me* L_{2,3}). Herein, *Me*-O hybridizations are included by admixing transitions of the type *Me* 2p⁶ 3dⁿ⁺¹ O 2p⁵ → *Me* 2p⁵ 3dⁿ⁺² O 2p⁵ (O 2p⁵ = \underline{L}), where a ligand-to-metal charge-transfer (LMCT) leads to a hole \underline{L} at oxygen sites. At the ligand sites, O 1s² O 2p^x → O 1s¹ O 2p^{x+1} (O K) are allowed transitions of the 1st order. Therefore NEXAFS at the *Me* L_{2,3} and O K edge provides useful information about the oxidation states of 3d metals and O 2 p states as well as about the electronic nature of the *Me*-O bonds.^{30,31} Ni and O are the main redox active elements in NCM111, NCM622 and NCM811 since the Ni L_{2,3} and O K NEXAFS spectra, recorded in fluorescence yield (FY) with a sampling depth of ~100 nm, show obvious differences between the charged and the discharged states (Figs. 1D–1F). The Co L_{2,3} and Mn L_{2,3} spectra do not reveal any differences between the two states of charge (see Appendix D) implying that Co and Mn do barely contribute to the charge compensation. Deviations from these findings reported in literature

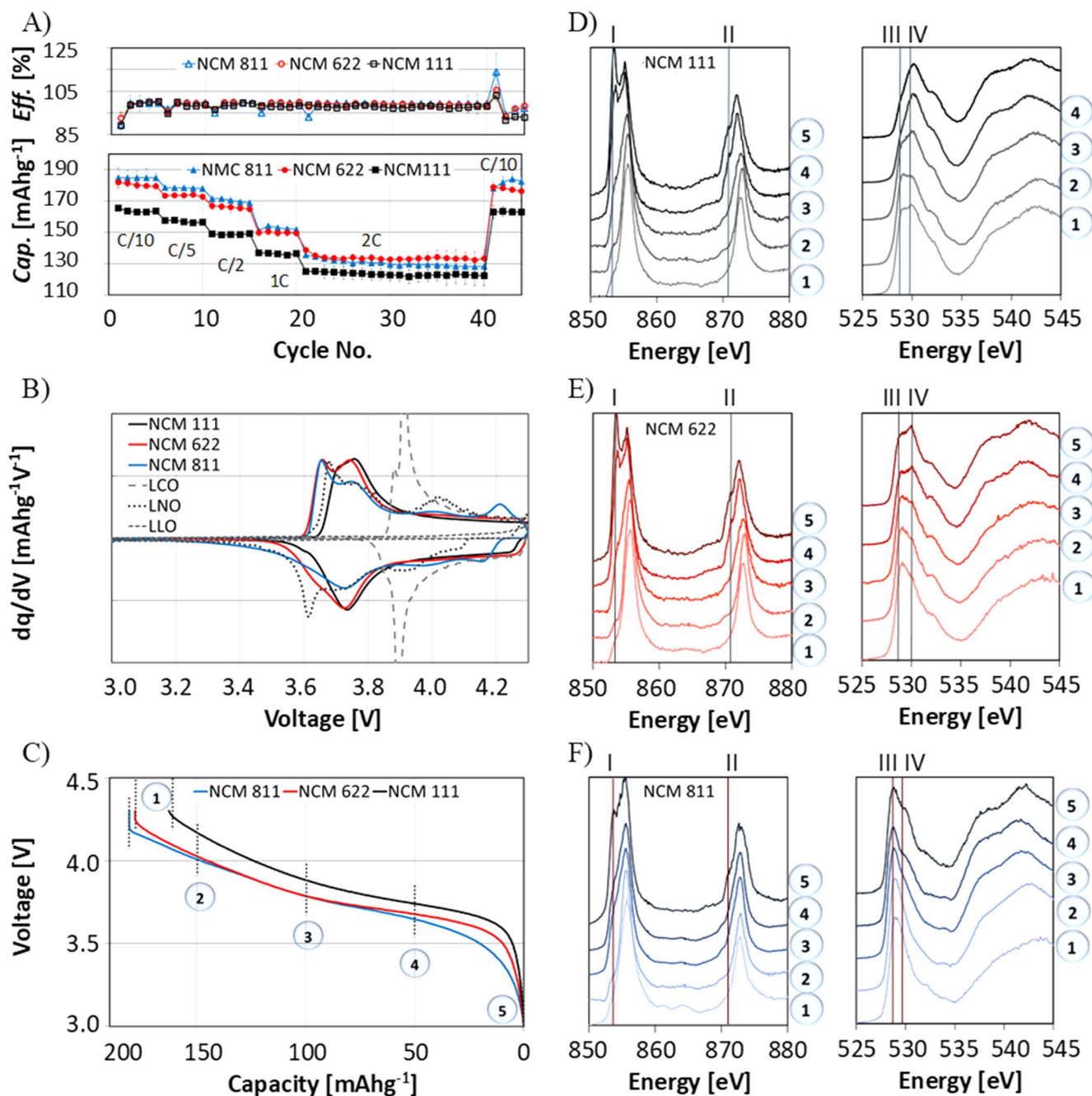


Figure 1. (A) Coulomb efficiency $Eff.$ and discharge capacity $Cap.$ of NCM111, NCM622 and NCM811. (B) Differential capacity (dq/dV) plot of the 1st NCM cycles in comparison to the reference materials LNO (LiNiO_2), LLO ($\text{Li}[\text{Li}_{1/3}\text{Mn}_{2/3}\text{O}_2]$) and LCO (LiCoO_2), measured with C/20 at 25 °C. (C) Voltage profile of the 1st discharge (C/20, 25 °C) of the NCMs. The numbers 1 to 5 mark the points at which NEXAFS data was taken. The NEXAFS data is shown in (D)–(F), with the Ni $L_{2,3}$ (1st diagram) and O K (2nd diagram) spectra of NCM111 (D), NCM622 (E) and NCM811 (F). The data is measured in fluorescence yield (FY).

can be due to (i) a difference in penetration depth of the applied detection mode. The surface of the NCM particles degrades much faster than the bulk, and surface sensitive measurements differ significantly from bulk measurements;^{63,64} (ii) A higher end of charge voltage leads to states of charge above the stability window of the materials, forcing at least partially irreversible reactions.^{46,47} Moreover, Co K and Mn K edges show significant changes at high states of charge which are mainly attributed to distortions and geometric effects in the local environment (the ligand field) of the elements and not to a change in the electronic configuration.^{28,65} In the case of Me K edge spectroscopy (hard X-rays, experimental setup does not require ultra-high vacuum), Me $1s^2 3d^n \rightarrow Me$ $1s^1 3d^{n+1}$ excitations are quadrupole transitions only allowed due to

distortions in the structure or/and vibrations of the atoms. Consequently, the peaks marking changes in the electronic configuration are relatively weak and Me $3d$ - O $2p$ interactions are often neglected upon data analysis. In the present work structural and electronic changes in the ligand field (O sites) are explicitly included using the charge transfer multiplet (CTM) theory while many NEXAFS studies simply relate shifts in peak positions, which can also have their origin in changes of the ligand field, to changes in the oxidation states of transition metals.

Upon discharge, low energy shoulders of the Ni L_3 (853 eV) and L_2 edge (871 eV) appear (Figs. 1D–1F, lines I and II) while O K peaks at 529 eV and 530 eV, which are assigned to excitations into O $2p$ states,^{23,36} are decreasing (Figs. 1D–1F, lines III and IV). The

Me $L_{2,3}$ edges are simulated with charge-transfer multiplet (CTM) calculations to extract changes in the valence states of the transition metals in the NCMs upon discharge, Fig. 2.^{25,30–32,64} CTM calculations are based on density functional theory (DFT) calculations of an infinite crystal. From these calculations a projection of the wavefunctions to a small cluster of the structure, in the present case to a

MeO_6 octahedron in the NCM host structure, is used to further calculate the complex *Me* spectra.^{31,32} Ligand-to-metal charge-transfer (LMCT) and core hole - valence electron (hole) interactions, which are unscreened in solids and need to be treated explicitly for all core states except K edges, are then solved for the cluster in an *ab initio* approach. CTM calculations have been performed over the

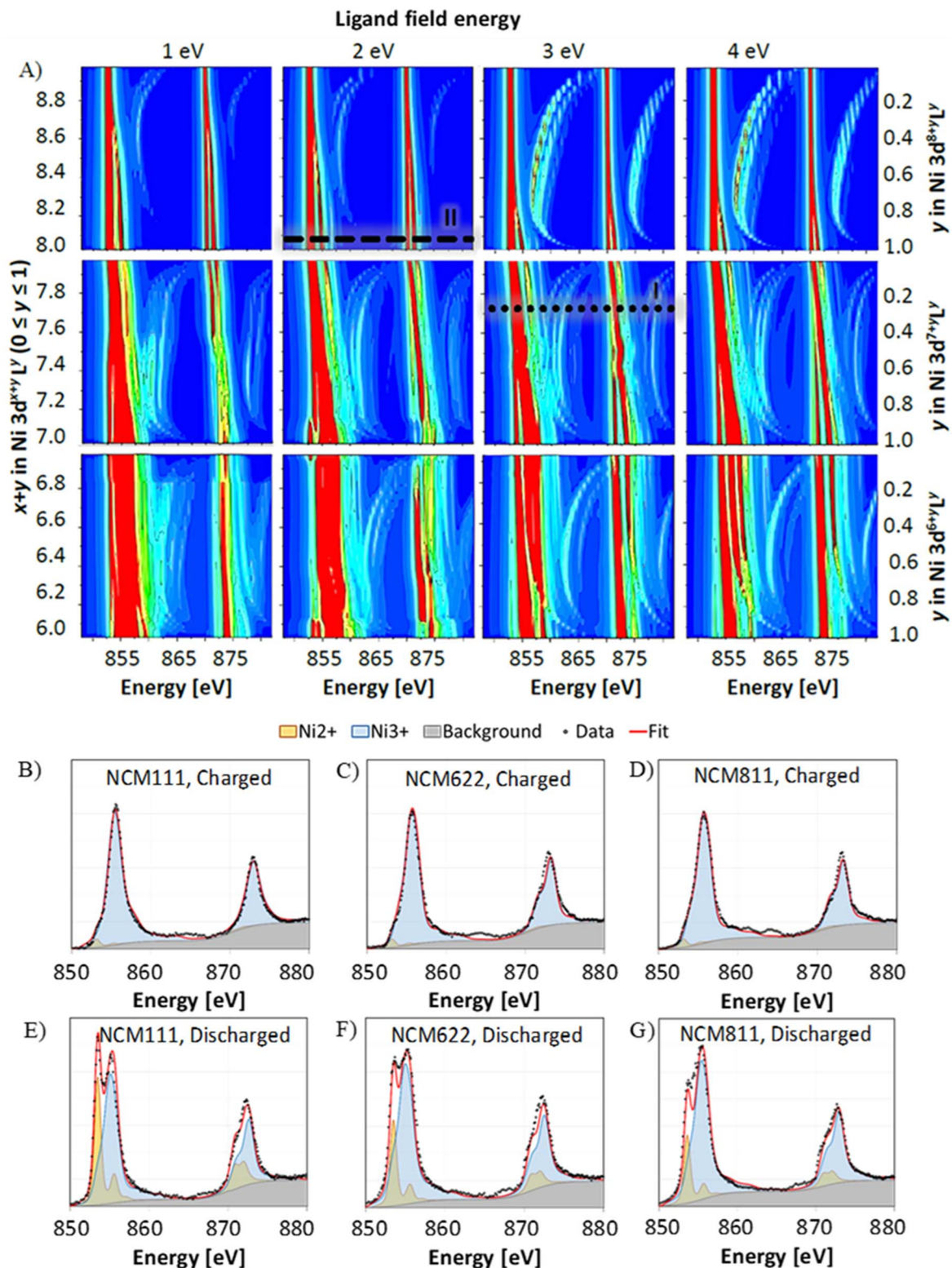


Figure 2. (A) CTM calculations of Ni $3d^x L^y$ ($x = 8, 7$ and $6, 0 \leq y \leq 1$, L denotes a hole at O $2p$ sites) varying the ligand-field energy from 1 eV to 4 eV and the charge-transfer-energy from -15 eV to 15 eV. (B-G) Measured (black dots) and simulated (red lines) Ni $L_{2,3}$ edge spectra of charged (B-D) and discharged (E-G) NCM111 (B, E), NCM622 (C, F) and NCM811 (D, G).

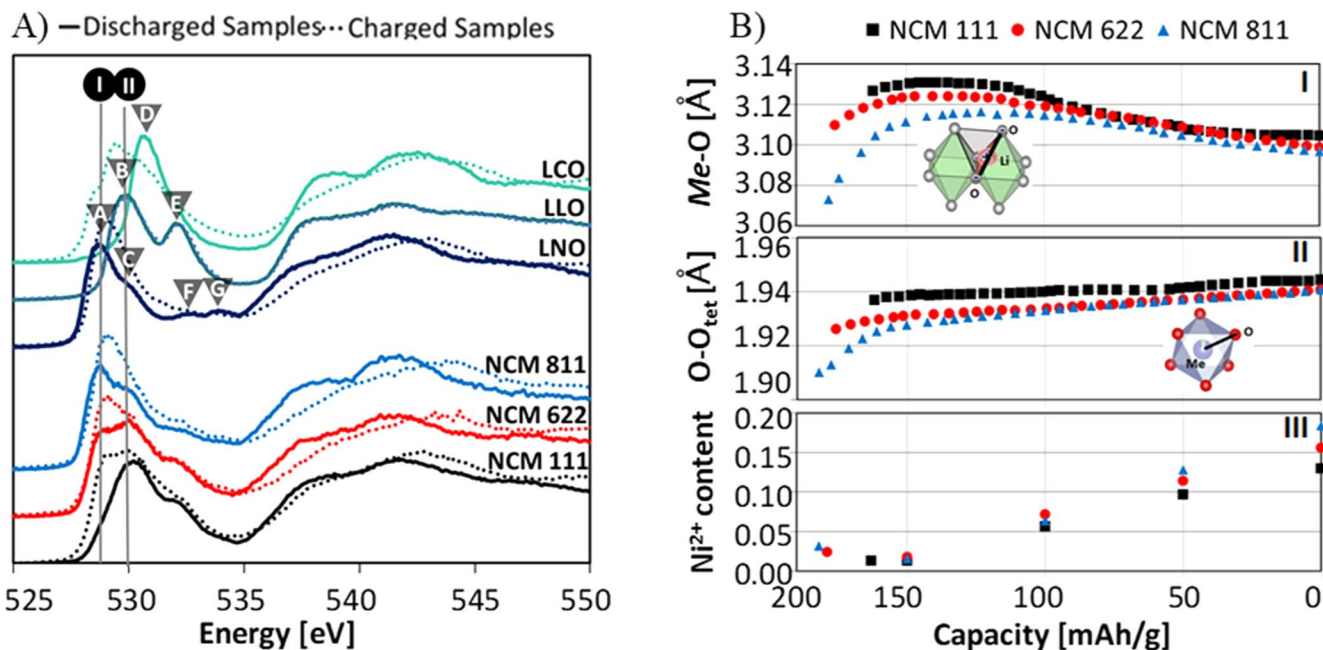


Figure 3. (A) O K NEXAFS spectra of NCM111, NCM622, NCM811, LNO (LiNiO₂), LLO (Li[Li_{1/3}Mn_{2/3}]O₂) and LCO (LiCoO₂) in the charged (solid line) and discharged states (dashed lines). (B) O-O_{tet} distances of the tetrahedral sites in the Li layer, Me-O distances of the MeO₆ octahedron as well as the Ni²⁺ content upon the 1st discharge.

last 30 years and have proven to describe *Me* $L_{2,3}$ edges in correlated systems such as the NCMs successfully.^{25,26,30–36,64} Fig. 2A gives an overview of the CTM calculations of Ni 3d^{x+y} \underline{L}^y with $x = 8$ (Ni²⁺, 1st row), $x = 7$ (Ni³⁺, 2nd row) and $x = 6$ (Ni⁴⁺, 3rd row). \underline{L} denotes a hole at O 2p sites and y , the probability with which the electron is transferred from an O ligand to Ni (LMCT). The LMCT can also be described with the chemical equilibrium Ni 3d^x $\underline{L} \rightleftharpoons$ Ni 3d^{x+1} \underline{L} where y would give the ratio of [Ni 3d^{x+1} \underline{L}]/([Ni 3d^{x+1} \underline{L}] + [Ni 3d^x \underline{L}]). If y equals 0.5, the probability to find the electron at Ni 3d or O 2p sites is 50% and the Ni–O bonds reach a maximum in covalence. For each x , y was varied from 0 to 1 by varying the LMCT energy from –15 eV to 15 eV in 1 eV steps.³⁰ From the 1st to the 4th column in Fig. 2A, the ligand-field (LF) energy was set to 1 eV, 2 eV, 3 eV and 4 eV, respectively. The core hole potential U_{pd} and the on-site Coulomb interactions U_{dd} were kept constant ($U_{pd} - U_{dd} = 1$ eV).

The best match of the charged NCM spectra and the CTM calculations is obtained for the Ni³⁺ configuration Ni 3d^{7.7} $\underline{L}^{0.3}$ with a LF energy of ~3 eV, Fig. 2A (dotted line I) and Figs. 2B–2D. The widely accepted cationic redox process ($Me^{2+ \text{ or } 3+} \rightleftharpoons Me^{4+} + 1$ or $2 e^-$) would suggest a Ni⁴⁺ configuration in the charged state.^{46,66–68} However, none of the calculated Ni⁴⁺ spectra show a good match with the measured data (see Appendix E). Moreover, it is well known that Ni³⁺ has a negative LMCT character which stabilizes the ligand hole character (the Ni 3d⁸ \underline{L} configuration) and therefore makes the formation of Ni⁴⁺ practically impossible.⁶⁹ Due to the LMCT the number of d-electrons around Ni in charged NCMs is 7.7 (Ni 3d^{7.7} $\underline{L}^{0.3}$) which does not differ much from Ni²⁺ (Ni 3d⁸, number of d-electrons = 8), the chemically preferred Ni configuration because of the half-filled e_g orbitals. Upon discharge the peaks which belong to the covalent Ni³⁺ configuration, are still present (shifted to slightly lower energies) but new peaks at 853 eV and 871 eV appear (Figs. 1D–1F, line I, II). These peaks are assigned to a very ionic Ni²⁺ configuration (Ni 3d^{7.96} $\underline{L}^{0.04}$, LF energy ~2 eV, Fig. 2A, dashed line I, II and Figs. 2E–2G). The Ni²⁺/Ni³⁺ ratio increases upon discharge from <4% for all NCMs to 42% for NCM111, 38% for NCM622 and 31% for NCM811, respectively. This means that the electronic structure changes from a very covalent (>96% of covalent Ni³⁺) in the charged state to a more ionic character (58%–69% of covalent Ni³⁺, 42%–31% of ionic

Ni²⁺) in the discharged state (Fig. 3A and Appendix D). The charge compensation (*via* a change in the covalence of Ni–O bonds) is only possible because of the high Ni²⁺ content in the discharged NCMs (> 30%). Note that sometimes it is assumed, that the Ni²⁺ content is in the order of the Li/Me disorder (roughly 2% to 5%, see *e.g.* ^{70,71}). While powder diffraction data confirms a Li/Me disorder of ~2% for all NCMs used in the present work (Appendix B, Fig. B 1G–L), the determined Ni²⁺ content is much higher. The presence of more than 30% Ni²⁺ in the discharged state can partially be explained by the 4 + configuration of the more electronegative Mn, determined with Mn $L_{2,3}$ NEXAFS and CTM calculations (Appendix D). However, there is more Ni²⁺ present in NCM622 and NCM811 than expected from the Mn content which might arise from an oxygen deficiency.⁶⁴

The probability to find a hole \underline{L} at O sites (Ni 3d^x $\underline{L} \rightleftharpoons$ Ni 3d^{x+1} \underline{L}) directly probes the O character of the NCM valence states and \underline{L} can be detected using O K edge NEXAFS (peaks between 528 eV and 532 eV,^{23,28,70}). The number of holes in O 2p orbitals decreases upon discharge (Figs. 1D–1F, line III, IV, from the bottom to the top) indicating a decrease in the covalent character of the Me–O bonds which is consistent with the Ni $L_{2,3}$ NEXAFS analysis. Comparing the O K edge spectra of charged and discharged NCM111, NCM622, and NCM811 to O K reference spectra of LNO (LiNiO₂), LLO (Li[Li_{1/3}Mn_{2/3}]O₂) and LCO (LiCoO₂) (Fig. 3A) helps to distinguish the individual contributions of Ni-, Co- and Mn–O hybridizations. The peaks A–E are O 1s (O K shell) core electron excitations into empty O 2p states.^{23,36} The hybridization of Ni and O orbitals leads to peaks at 529 eV (peak A) and 530 eV (peak C) as evident from the pre-peaks in the O K spectra of discharged LNO. One Co–O peak in the discharged LCO spectrum is found at 531 eV (peak D) while electronic holes from the Mn–O hybridization (discharged LLO) lead to peaks at 530 eV and 532.5 eV (peak B and E). The peaks at energies around 534 eV (peak F and G) are assigned to electron excitations into Hubbard bands²⁸ and the broader peaks above 535 eV to transitions into hybridized states of O 2p and Me 4s or higher unoccupied *Me* orbitals.^{23,28,70} The changes in the O K NCM spectra upon charge are comparable to changes observed for LNO (Fig. 3A), confirming that mainly Ni contributes to the charge compensation of layered oxides which agrees with the results from the dq/dV plots and the *Me* $L_{2,3}$ NEXAFS analysis.

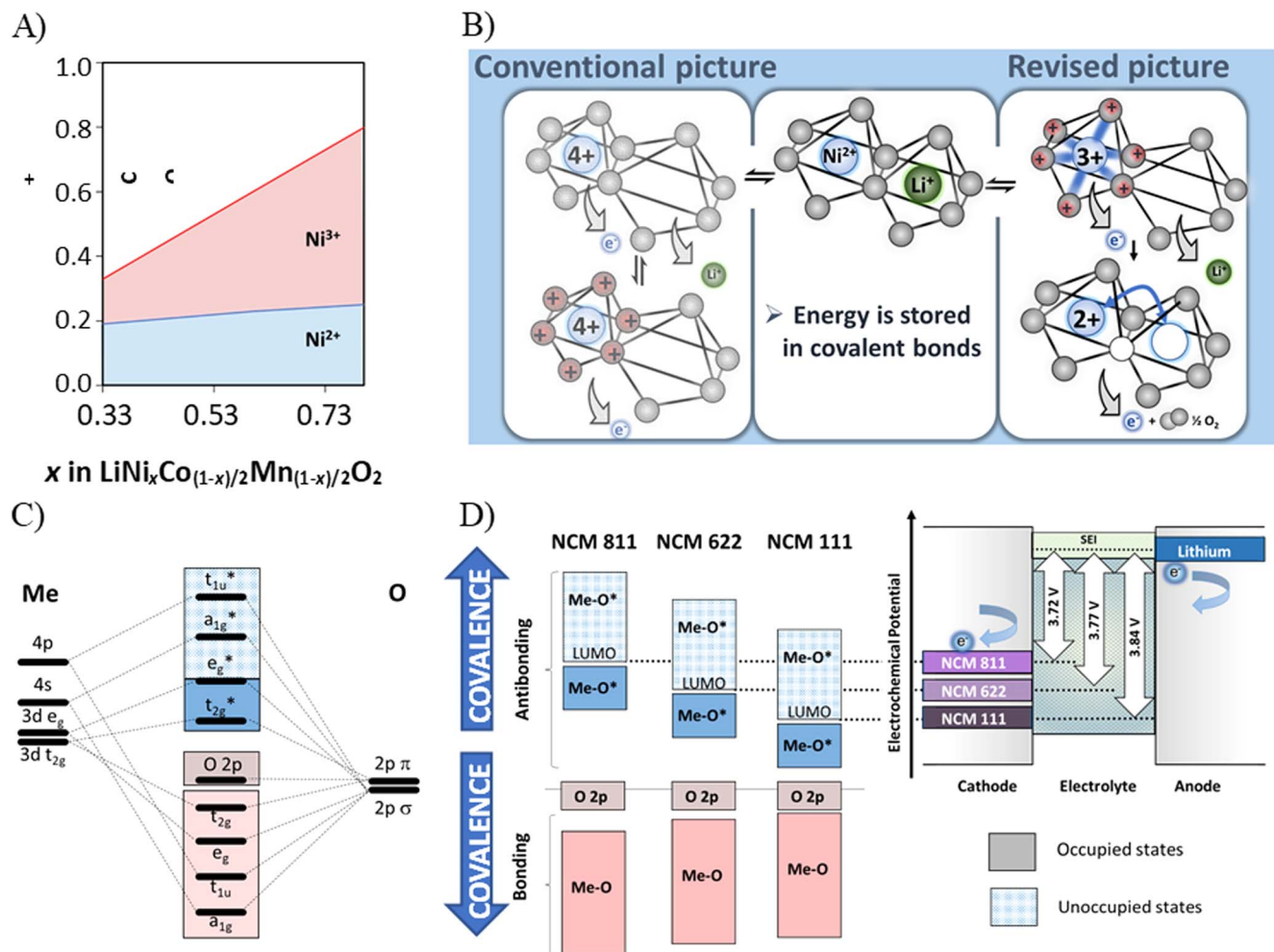


Figure 4. (A) Relative Ni^{2+} and Ni^{3+} content in dependence on the overall Ni content in NCM. (B) Depiction of the conventional and revised redox process in NCMs. (C) Molecular orbital scheme of Ni in an O octahedron, and (D) electrochemical potential of the NCMs in dependence on the covalence of the Me-O host structures.

These results also question that O is reversibly redox active in the Me-O host structures at high states of charge (“anionic redox” or “lone state” redox activity) as it was found for Li-rich materials.^{42,71} The electron density at oxygen sites decreases due to the formation of covalent bonds with its Ni neighbors and not independent of any transition metal due to the redox process $\text{O}^{2-} \rightleftharpoons \text{O}^{(-2+x)-} + x e^-$ ($0 < x < 1$).^{43–45} When Tarascon et al. first shaped the term “anionic redox,” it described indeed redox processes affiliated with Me-O hybrid orbitals.³⁷

The electronic changes in Li_xMeO_2 , deduced with NEXAFS, are highly correlated to crystallographic changes which are investigated with *operando* synchrotron X-ray powder diffraction (SXPD). The interstitial sites upon Li-diffusion are the tetrahedral sites in the Li layer and the edge length of these tetrahedra ($\text{O}-\text{O}_{\text{tet}}$, Fig. 3B I), which follows the c lattice parameter (Fig. C-3E, Appendix C), in turn defines the activation barrier for Li motion.^{72,73} The smaller the tetrahedra, the larger the attractive interactions between Li and O and thus the higher the activation barriers for the migration process. Upon discharge repulsive interactions between negatively charged, opposing oxygen layers decrease as Li ions, the positive charges placed between the layers, are inserted. This leads to a decreasing size of the tetrahedral sites and thus to an increase in the activation barrier which is found from $\sim 155 \text{ mAh g}^{-1}$ to the discharged state. At the same time, the Me-O distances (Fig. 3B II) and the a, b -lattice parameters (Fig. C-3C, Appendix C) increase which is consistent with the decreasingly covalent character of the Ni-O bonds.

The redox processes and crystallographic changes observed between the charged state and $\sim 155 \text{ mAh g}^{-1}$ are more complex. The present picture suggests that Van der Waals interactions between Li vacancies in adjacent Li layers, as e.g. derived from DFT calculation,⁷⁴ drive the crystallographic changes (increasing $\text{O}-\text{O}_{\text{tet}}$ and Me-O distance) in this region. However, these calculations rely on the assumption that all transition metals in LiMeO_2 ($\text{Me} = \text{Ni}, \text{Co}, \text{Mn}$) reach a 4+ oxidation state which contrasts with the above findings: Only Ni and O are redox active, Ni does not reach a 4+ oxidation state upon charge and Ni is slightly oxidized from a less to a more covalent configuration from the charged state to 155 mAh g^{-1} ($\text{Ni}^{2+} \rightarrow$ covalent Ni^{3+} , Fig. 3B III). This is evident from the decreasing Ni^{2+} peaks in the Ni $L_{2,3}$ spectra (853 eV and 871 eV) and the increasing Ni-O hybrid peaks in the O K spectra (529 eV and 530 eV), Figs. 1D–1F (spectra 1 and 2) and Fig. F-1D–F-1I (Appendix F). Thus, the expectation that the extracted electrons arise from Me reduction is wrong. This goes along with the fact, that at 155 mAh g^{-1} the amount of Ni^{2+} is suppressed to almost zero (Fig. 3B III, the corresponding simulations are shown in Fig. D-1, Appendix D) ruling out that the reversible $\text{Ni}^{2+} \rightleftharpoons$ covalent $\text{Ni}^{3+} + e^-$ reaction can continue above 155 mAh g^{-1} upon charge.

The contrary development of the Me-O distances and the Ni^{2+} content between the charged state and 155 mAh g^{-1} , which means that the Me-O bond length is increasing although the Me-O host structures become more covalent, suggests that O depletion from surface near regions of the NCM particles upon charge and the partially reversible process upon discharge ($\text{MeO}_2 \leftrightarrow \text{MeO} + \frac{1}{2} \text{O}_2$

+ 2e⁻) followed by *Me* migration into Li sites, *Me* dissolution and phase transformations from the rhombohedral *via* a spinel like towards a rock salt type structure, are the underlying processes.^{13,16} These crystallographic changes also alter the O–O_{tet} distances as discussed above. Indeed, beside a breakdown in diffusion kinetics which is related to the breakdown of the O–O_{tet} distance above 155 mAh g⁻¹ (Table F 1, Appendix F and Refs. 73, 75) irreversible reactions like gas formation, surface reconstruction and transition metal dissolution are frequently reported (Table F-I, Appendix F and Refs. 76–78). Note that only a tiny amount of O released from the *Me*O₂ host structures is necessary to explain the capacity above 155 mAh g⁻¹ since this comes along with electrolyte decomposition,^{15,42,79,80} although it remains widely unclear to which extent the reversible Li de-/intercalation continues. 10–30 mAh g⁻¹ of the capacity are reported to arise from gas evolution reactions at high states of charge assuming that two to four electrons per O₂, CO and CO₂ are contributing to the charge compensation.^{15,42,76,80} The numbers slightly decrease for the subsequent cycles as the capacity of the NCMs does (Fig. 1A).^{15,80}

The collapse of the tetrahedral sites from 155 mAh g⁻¹ to the charged state (from the right to the left in Fig. 3B I) is much stronger in the case of NCM811 compared to NCM622 and NCM111, which can be related to the covalent character of the host structure. From NCM111 *via* NCM622 to NCM811 the covalent Ni³⁺ content increases from 14% to 37% and finally to 55% in the discharged NCMs (32%, 57% and 77% in the charged materials), Fig. 4A. The covalence seems to stabilize higher oxidation states and thus enables a higher degree of delithiation upon charge. However, the extent of irreversible reactions, especially on the surface of the particles, is also prone to increase at a higher degree of delithiation and at a related larger absence of ionic Ni²⁺, which shortens the material lifetime (Appendix C and Appendix F).¹⁵

Discussion

Knowing the reversible charge exchange reaction in NCMs helps to unravel physical limitations. Theoretically one mole Li ions and one mole electrons can be extracted per mole Li*Me*O₂ upon charge (Li*Me*O₂ ⇌ *Me*O₂ + Li⁺ + e⁻). However, at *x* < 0.56 in Li_{*x*}*Me*O₂ (states of charge > 155 mAh g⁻¹), NCMs undergo irreversible reactions (see Appendix F). At this point, the Ni²⁺ content is suppressed to zero which suggests that Ni²⁺ present in the discharged NCMs limits the reversible capacity. In other words, the reversible reaction is the reaction of ionic Ni²⁺ to covalent Ni³⁺ (upon charge) and *vice versa* upon discharge and a revised picture of reversible and irreversible processes in NCMs is given in Fig. 4B. The findings above imply that if there is a way to increase the available amount of Ni²⁺, *e.g.*, by substituting *Me* or O with stronger electron donating cations or anions, the reversible capacity (which is determined by the point where Ni²⁺ is suppressed to zero) would increase along with it.^{81–83}

The degree of covalence of the NCMs is also a key determinant of the electrochemical potential and thus the electrode potential and cell voltage (Figs. 4C and 4D), *i.e.* apart from the capacity, it is the second most important parameter for the energy density of Li ion batteries. Fig. 4C shows a molecular orbital scheme of Ni in an octahedral O environment as deduced in Ref. 31. Please note that this depiction does not put emphasis on the band gap between the highest occupied molecular orbital (HOMO) and the lowest unoccupied molecular orbital (LUMO) nor is it related to the nature (*e.g.* insulator, semiconductor, metal) of the cathode material (determined by *U_{dd}* and the LF energy). It just depicts the stabilization of bonding and destabilization of antibonding states in an NiO₆ octahedron as the driving force for covalent interactions between Ni and O orbitals.^{84,85} As it was proven with O K NEXAFS, the non-bonding O 2p states do not participate in the charge compensation and their relative energetic position is randomly chosen. The spontaneous reaction of layered oxides is the intercalation of Li-ions, which is the discharge reaction. This implies that electrons are

taken out of the HOMO of the anode and are filled into the LUMO of the cathode (e⁻ and blue arrows, Fig. 4D).^{49–51} Therefore, the LUMOs of the NCMs define the redox potential of the cathodes and thus the open cell voltage of the batteries.^{49–51} The LUMOs of the NCMs, in turn, are antibonding *Me*–O* states as deduced with NEXAFS. With an increasingly covalent character, the bonding states decrease while the antibonding states increase in energy, as depicted in Fig. 4D. With the antibonding states the HOMOs and LUMOs shift up in energy with increasing covalent interactions and the mean charge and discharge voltage decreases (Fig. 4D). Due to the disproportionately high increase of covalent Ni³⁺ from NCM111 (14%) *via* NCM622 (37%) to NCM811 (55%), Fig. 4A, the covalent character of the materials increases and thus the mean discharge voltage decreases (NCM111: 3.85 V, NCM622: 3.79 V, NCM811: 3.75 V). The mean discharge voltages are determined using the galvanostatic intermittent titration technique (GITT, for more details see Appendix G) to minimize kinetic effects on the values discussed. Reducing the amount of covalent Ni³⁺ in pristine NCMs would therefore lower the LUMOs, leading to higher mean discharge voltages.

Conclusions

In electrochemical devices energy is stored in chemical bonds—that this is not only true for fuel cells and electrolyzers but for Li ion batteries as well is shown in the present work: Reversible charge compensation in NCMs proceeds from Ni²⁺ to Ni³⁺ while electron density is shifted from O towards Ni forming covalent Ni–O bonds. The high energy densities of NCMs are thus obtained due a change in covalence of Ni–O bonds. A main conclusion from these findings is that the ability to increase the Ni²⁺ content without increasing the amount of more covalent Ni³⁺ will lead to outstanding capacities AND voltages. Thus, the physical limits of conventional cathode materials can still be pushed without the need of massive changes in cell chemistry.

Acknowledgments

Financial support was provided by the Federal Ministry of Education and Research (BMBF) under the funding number 03XP0231. We wish to acknowledge KARA and the KNMF (both Karlsruhe, Germany), as well as the Diamond Light Source (UK, proposal NR19772 and SI22706) for provision of beamtime. We also acknowledge Christoph Suergers for the provision of the transfer chamber which enabled us to transfer our samples from the Glovebox into the load lock of the WERA beamline at KARA without any contact to air.

Appendix A. Impact of Electrolyte Decomposition Products and Binder on XAS Spectra

Decomposition products deposited on/as the cathode electrolyte interphase are mainly Li salts like carbonates, fluorides, or phosphates.⁸⁶ Carbonates and phosphates lead to additional peaks in the O K spectra (at ~533 eV and ~535 eV, respectively^{87,88}) while the F K edge appears at ~698 eV with EXAFS features at higher energies interfering with the Co *L*_{2,3} and Ni *L*_{2,3} edge. Fluorine is also present in the materials due to PvdF (binder, see experimental section). An overview spectrum of NCM111 (100 cycles, C/2, 2.0 V and 4.6 V) before and after rinsing with dimethyl carbonate (DMC) for 5 min (Fig. A-1A) is provided for three reasons: (i) To ensure that the O K edge peaks in the FY spectra are correctly attributed to either the bulk material or to electrolyte decomposition products, (ii) to prove to which extent the Co *L*_{2,3} and Ni *L*_{2,3} edges are affected by the F K edge EXAFS features and (iii) to figure out, whether rinsing can help to minimize these effect. The F K edge dominates the overview spectra showing that fluorine (stemming from electrolyte decomposition products or binder) is the main component present in the cathode electrolyte interphase. It also becomes obvious that rinsing the sample with DMC does not reduce the amount of fluorine since the intensity of the F K edge does not decrease. To reveal the effect of decomposition

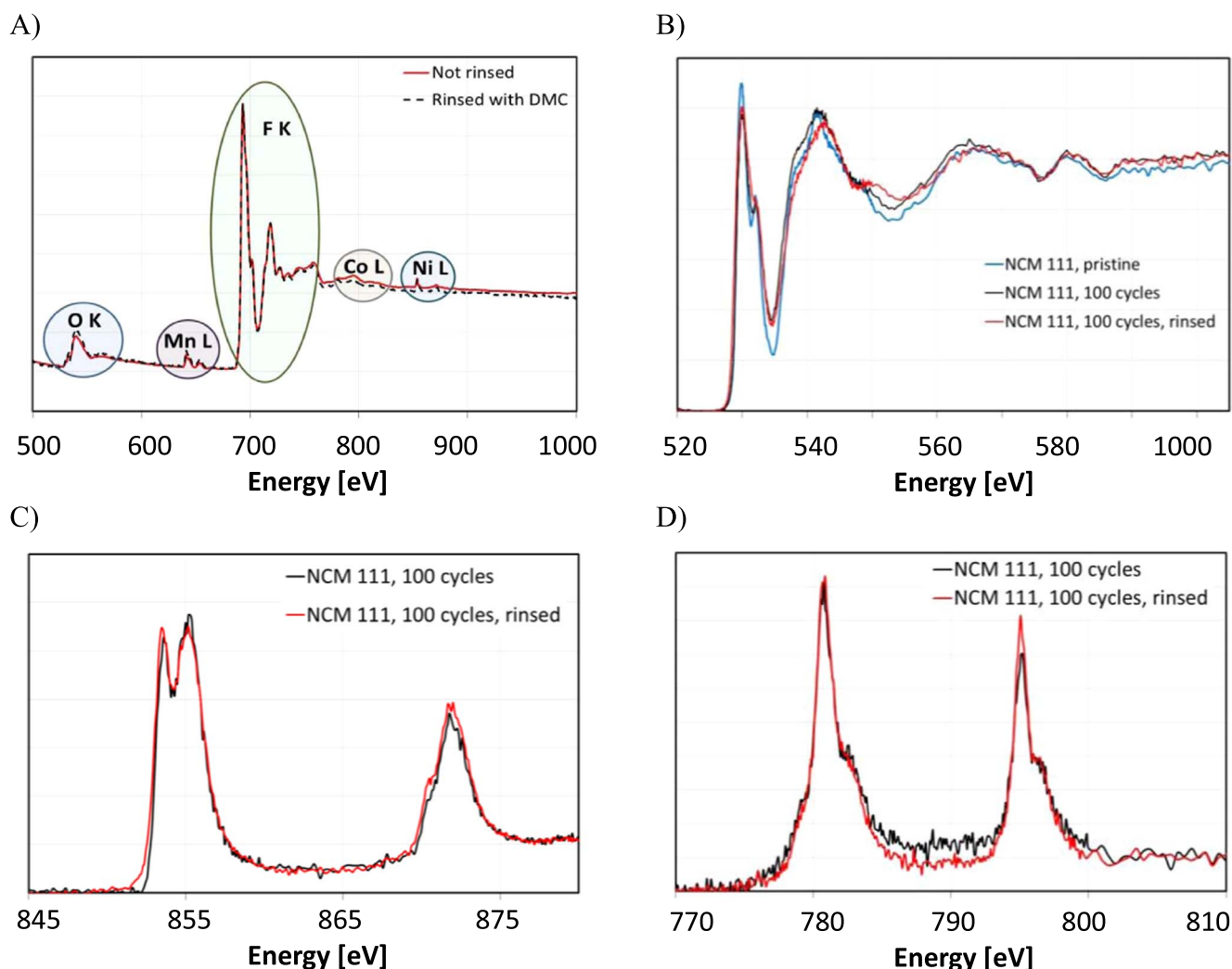


Figure A-1. (A) Overview spectra of NCM111 (TEY signal/I₀) after 100 cycles (red, solid line) and rinsed with DMC for 5 min (black, dashed line). (B) FY O K NEXAFS of pristine NCM111 (blue line), NCM111 after 100 cycles (black line) and NCM111 after 100 cycles and rinsed with DMC for 5 min in an argon filled glovebox. (C) Ni $L_{2,3}$ and (D) Co $L_{2,3}$ edge of NCM111 after 100 cycles (black lines) as well as after rinsing (red lines).

products on the O K spectra, Fig. A-1B shows the FY O K spectra of pristine NCM111, NCM111 after 100 cycles as well as NCM111 after 100 cycles and rinsed for 5 min with DMC. No additional peaks are found comparing pristine NCM111 (which was not exposed to electrolyte) with NCM111 after 100 cycles, no matter if the sample was rinsed or not. The absence of peaks at 533 eV and 535 eV, where O K peaks of LiNiPO_4 and Li_2CO_3 are expected^{87,88} further confirms that the effect of surface impurities can be neglected considering FY spectra. Figs. A-1C and A-1D show FY spectra of the Ni $L_{2,3}$ and Co $L_{2,3}$ edge of NCM111 after 100 cycles (black: without rinsing, red: with rinsing). As discussed, rinsing does not lead to significant changes. Nevertheless, it must be mentioned that the EXAFS features of the F K edge overlap significantly with the Co $L_{2,3}$ and to a minor extent with the Ni $L_{2,3}$ edge leading to difficulties in the background correction of the spectra. Therefore, the slope of the background was determined using an energy range after the L_2 edges. The line was then positioned into the minimum before the edge jump (average of 5 points around the minimum in intensity before the onset of the L_3 edge).

Appendix B. Pristine NCMs

Scanning electron microscopy (SEM) pictures of NCM111 (Figs. B-1A, B-1D), NCM622 (Figs. B-1B, B-1E) and NCM811 (Figs. B-1C, B-1F) are measured using a Hitachi TM-1000 table top instrument. The samples show spherical secondary particles with a

size of around $10\ \mu\text{m}$. The size of the primary particles can hardly be determined from these images. The Brunauer, Emmett, Teller (BET) surface for NCM111 ($0.41\ \text{m}^2\ \text{g}^{-1}$), NCM622 ($0.34\ \text{m}^2\ \text{g}^{-1}$) and NCM811 ($0.36\ \text{m}^2\ \text{g}^{-1}$) was determined using a Quantachrome autosorb[®] iQ system. Please note that the surface area of layered oxides can increase up to 50% upon long-term cycling due to crack formation and in relation to that, the differences in the BET area observed for the pristine materials are small.⁸⁹ Layered oxides crystallize in the space group $R\bar{3}m$ in which Li ions and transition metals occupy edge-sharing oxygen octahedra in alternating layers. Figs. B-1G–B-1I shows the powder diffraction patterns of NCM111, NCM622, NCM811 collected at beamline I11 with the high-resolution MAC detector⁹⁰ which can probe impurities with a phase content $\leq 2\%$. The energy of the X-ray beam was tuned to 15 keV and the calibrated wavelength was $0.825270(10)\ \text{\AA}$. The pristine materials are measured in a borosilicate capillary (0.5 mm outer diameter) and the 2D data was rebinned to a step size of 0.005° using a Diamond software. The refinement was performed as described in the experimental section. The corresponding refinements confirm that the obtained powders are phase pure. The obtained crystallographic data is given below the refinements, Figs. B-1J–B-1L. With an increasing Ni content x in $\text{LiNi}_x\text{Co}_{(1-x)/2}\text{Mn}_{(1-x)/2}\text{O}_2$ the a , b lattice parameter increases while the c lattice parameter decreases. The mean Li/Me disorder is 2.5% for NCM111, 2.1% for NCM622 and 2.4% for NCM811. The primary particles are larger than 300 nm

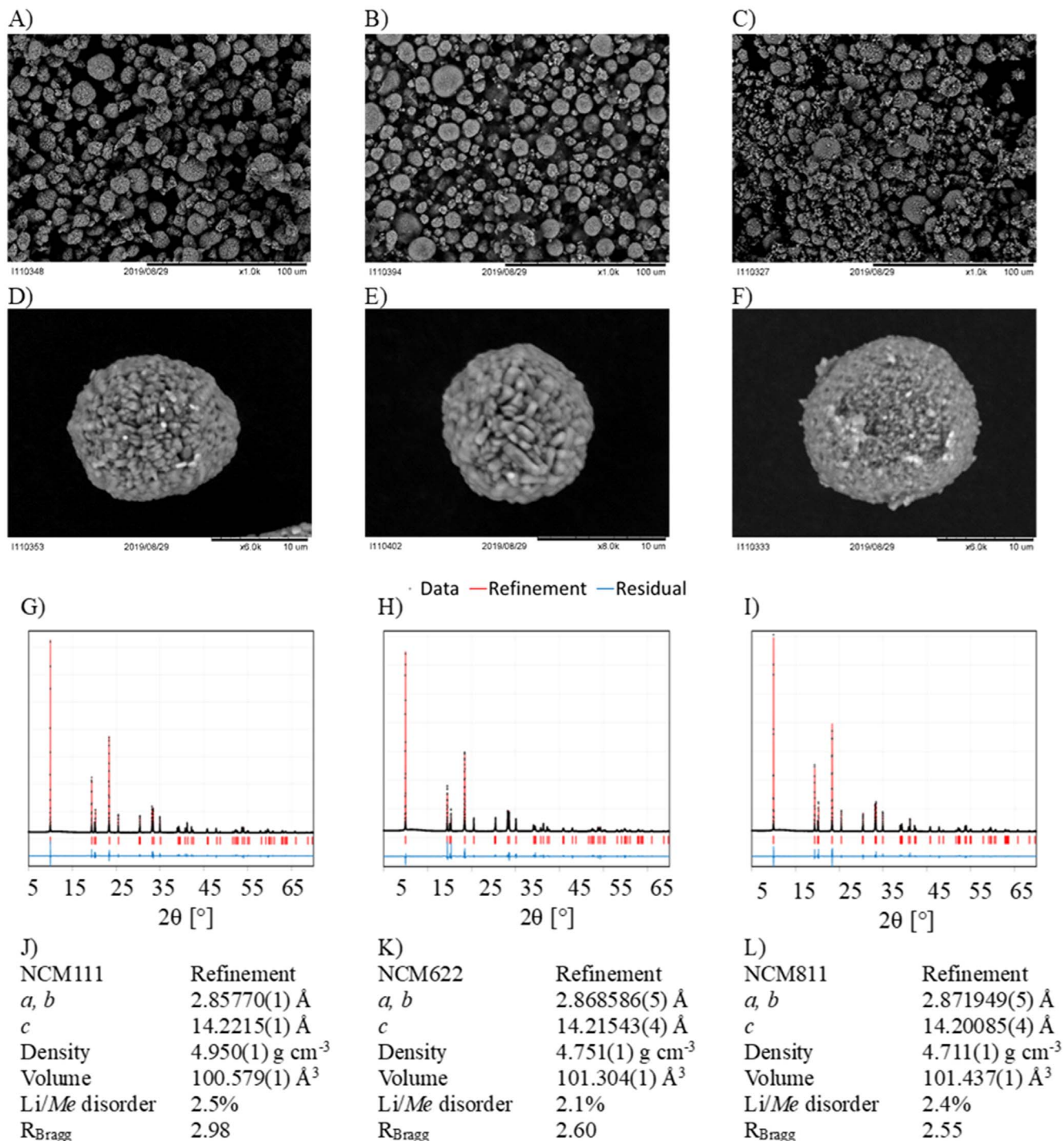


Figure B-1. SEM pictures of NCM111 (A), (D), NCM622 (B), (E) and NCM811 (C), (F). (G) to (I) show powder diffraction data and refinements ((G): NCM111, (H): NCM622 and (I): NCM811) collected at beamline 111 with the MAC detector. The crystallographic information obtained from the refinements is given below ((J): NCM111, (K): NCM622, (L): NCM811).

(powder diffraction and Rietveld refinement) but since the reflection broadening is dominated by microstrain and instrumental broadening, the exact size cannot be derived.

Appendix C. Long Term Performance of NCM111, NCM622 and NCM811

Fig. C-1 shows the cycling performance of NCM111, NCM622 and NCM811 over 84 cycles. For this data the rate test shown in Fig. 1 (main text) is repeated 2 times with 3 cells (2 x (5 x C/10, 5 x

C/5, 5 x C/2, 5 x 2C, 20 x 1C) + 5 x C/10). Cycling is performed at 25 °C between 3.0 V and 4.3 V. Figs. C-1A and C-1B give and overview of the mean discharge capacity and the corresponding cycling efficiency of the cathodes in dependence on the cycle number, Figs. C-1C–C-1H show the voltage profile (C-1C, C-1E and C-1G) and the dq/dV plot (C-1D, C-1F and C-1H) of the 2nd, the 42nd and the 82nd C/10 cycle. The cycling performance of NCM111, NCM622 and NCM811 is compared to data reported in literature (Table C-1). The initial discharge capacity between 3.0 V and 4.3 V of NCM111 is 163 mAh g⁻¹. The reported values with the

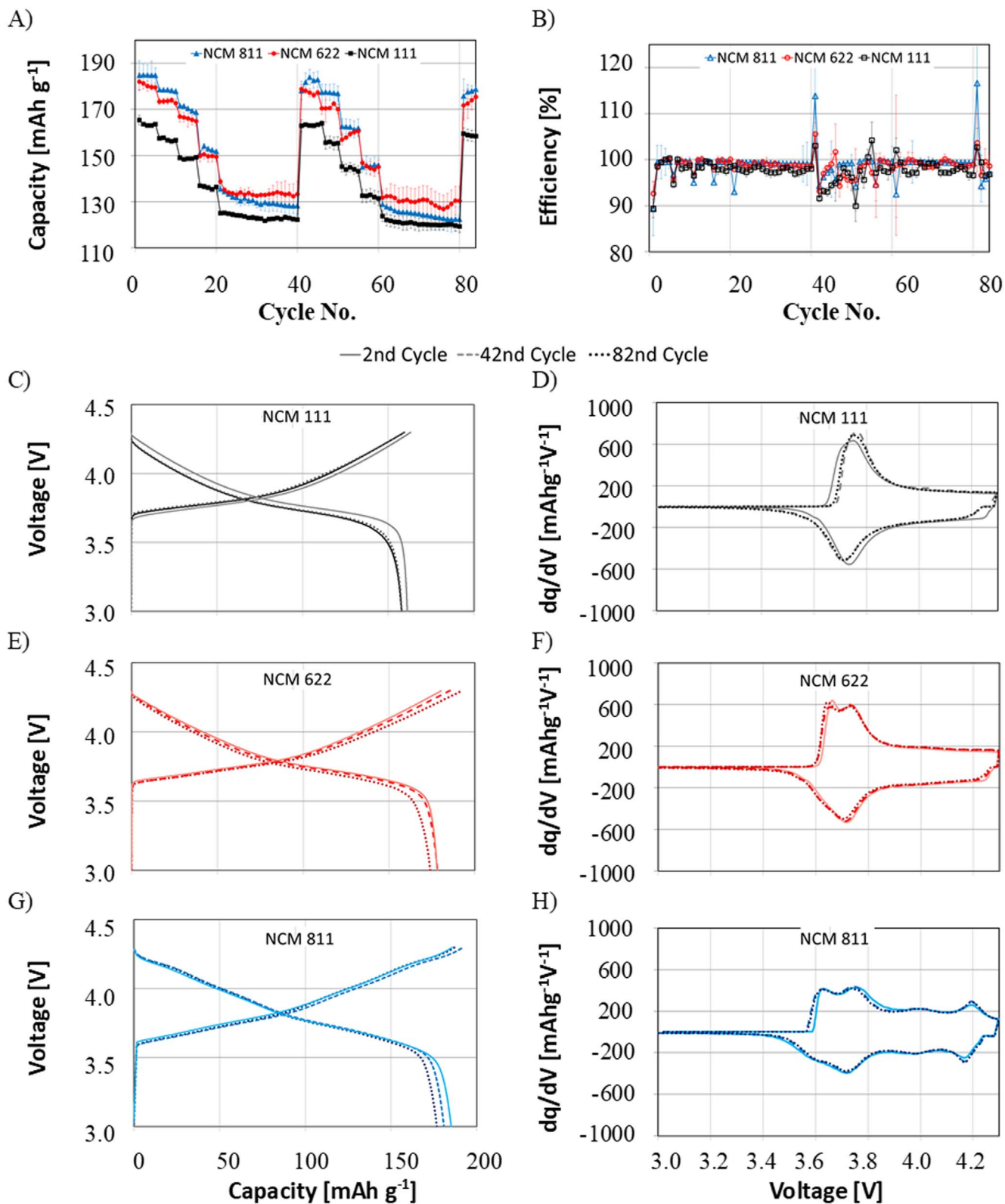


Figure C-1. Long term performance of NCM111, NCM622 and NCM811 with (A), mean discharge capacity and (B) cycling efficiency obtained with the following cycling procedure: 2 x (5 x C/10, 5 x C/5, 5 x C/2, 5 x 2C, 20 x 1C) + 5 x C/10 at 25 °C between 3.0 and 4.3 V. (C), (E) and (G) show the voltage profile, (D), (F) and (H) the differential capacity dq/dV of the 2nd, the 42nd and the 82nd cycle of NCM111 (C, D), NCM622 (E, F) and NCM811 (G, H).

same cutoffs range from 145 mAh g^{-1} to 155 mAh g^{-1} but by increasing the end of charge voltage to 4.6 V, capacities of up to 170 mAh g^{-1} can be achieved. NCM622 offers a discharge capacity of around 182 mAh g^{-1} , the corresponding literature values range from

175 mAh g^{-1} to 182 mAh g^{-1} (190 mAh g^{-1} with a cutoff voltage of 4.6 V). The initial discharge capacity of NCM811 corresponds with 186 mAh g^{-1} to the lower values of the values reported in literature (184 mAh g^{-1} -210 mAh g^{-1}).

Table C-I. Discharge capacities of NCM111, NCM622 and NCM811 reported in literature.

References	Cycling	Cy. No., C-rate	NCM111 [mAh g ⁻¹]	NCM622 [mAh g ⁻¹]	NCM811 [mAh g ⁻¹]
Qian et al. J. Mater. Chem. A, 7, 12723 (2019): Figs. 6a–6d	2.8–4.3 V	1, 0.2C	150	178	184
	Li NCM	80, 0.2C	145	140	184
Evertz et al. Anal. Bioanal. Chem. 411, 277–285 (2019): Fig. 1	3.0–4.6	1, 0.2C	170	190	210
	Li NCM	55, 1C	150	150	175
De Biasi et al. J. Phys. Chem. C. 121, 26163 (2017): Fig. 2a	3.0–4.3 V	1, 0.1C	155	178	187
	Li NCM	—	—	—	—
Jung et al. J. Electrochem. Soc. 164, A1361 (2017): Figs. 1–3	3.0–4.2V	1, 0.1C	150	176	190
	graphite NCM	80, 1C	140	158	160
Kondrakov et al. J. Phys. Chem. C. 121, 24381 (2017): Fig. 1	3.0–4.3 V	1, 0.5C ^{a)}	—	—	210
	Li NCM	50, 0.5C ^{a)}	—	—	178
Duan et al. Adv. Mater. 31, 1807789 (2019): Figs. 4b, 4d	2.8–4.3 V	1, 0.2C ^{b)}	—	182	185
	Li NCM	80, 0.2C ^{b)}	—	160	180
Friedrich et al. J. Electrochem. Soc. 166, A3760 (2019): Fig. 2	3.0–4.5 V	1, 0.1C	—	—	208
	Li NCM	80, 0.5C	—	—	170
Xu et al. Nat. Mat. 20, 84 (2021): Extended Data Fig. 1	2.5–4.2V	1, 0.05C	—	—	192
	graphite NCM	80, 0.05C	—	—	187
Märker et al. Chem. Mater, 31, 2545: Fig. 1	3.0–4.4V	1, 0.05C	—	—	205
	Li NCM	—	—	—	—
Laszczynski et al. J. Electrochem. Soc.166, A1853 (2019): Fig. 1.	3.0–4.2V	1, 0.5C	—	—	184
	graphite NCM	80, 0.5C	—	—	170
Zheng et al. ACS Appl. Energy Mater. 3, 2837 (2020): Fig. 2d	3.0–4.3 V	1, 0.1C	—	—	180
	Li NCM	80, 0.1C	—	—	170
Zhang et al. ACS Sustain. Chem. Eng. 8, 9875 (2020): Fig. 4d	3.0–4.3 V	1, 0.05C	—	180	—
	Li NCM	80, 2C	—	135	—
Tao et al. Ceram. Int. 43, 15173 (2017): Fig. 3b	2.8–4.3 V	1, 0.1C	—	178	—
	Li NCM	80, 0.1C	—	160	—
Kremer et al. Batter. Supercaps. 3, 1172 (2020): Fig. 5b	3.0–4.3 V	1, 0.1 C	—	175	—
	Li NCM	—	—	—	—
Yao et al. Mater. Today Commun. 19, 262 (2019): Fig. 4b	2.8–4.3 V	1, 1C	—	175	—
	Li NCM	80, 1C	—	125	—
Kim et al. Energy Environ. Sci. 11, 1449 (2018): Fig. 2a	3.0–4.3 V	1, 1C ^{b)}	—	—	200
	Li NCM	—	—	—	—
Kim et al. Energy Environ. Sci. 11, 1449 (2018): Fig. 2c	2.8–4.2 V	1, 1C	—	—	160
	graphite NCM	80, 1C	—	—	144
Doo et al. ACS Appl. Energy Mater. 2, 6246 (2019): Fig 8a	3.0–4.4V	1, 0.5C	—	—	210
	Li NCM	80, 0.5C	—	—	190
Woo et al. J. Electrochem. Soc. 154, A1005 (2007): Fig. 3b	3.0–4.3 V	1, 0.5C ^{a)}	—	—	210
	Li NCM	80, 0.5C ^{a)}	—	—	182
Noh et al. J. Power Sources. 233, 121 (2013): Fig. 4a	3.0–4.3 V	1, 0.5C	—	—	190
	Li NCM	80, 0.5C	—	—	170

a) Elevated temperatures. b) Different charge and discharge rate.

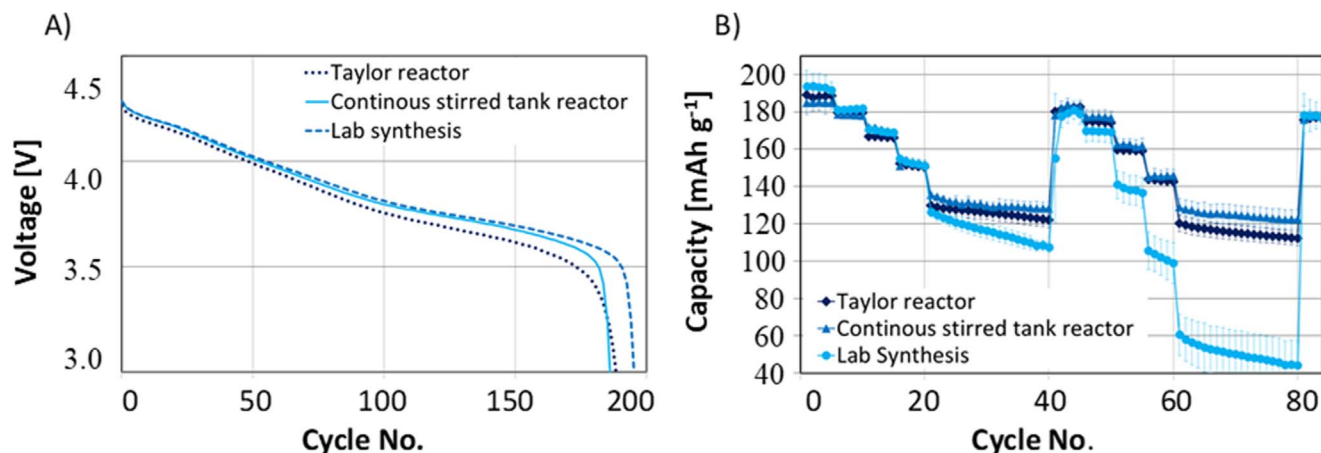


Figure C-2. Initial discharge capacity (A) and long term performance (B) of NCM811 synthesized using a laminar tank reactor, a batch reactor, and a lab synthesis route. The cycling procedure for (B) was as follows: 2 x (5 x C/10, 5 x C/5, 5 x C/2, 5 x 2C, 20 x 1C) + 5 x C/10 at 25 °C between 3.0 and 4.3 V.

To investigate the initially low discharge capacity of NCM811 and explore possible pathways to improve the cycling performance of the material, the synthesis route was changed, Fig. C-2. Instead of using a continuous stirred tank reactor^{52,53} for the precipitation of the $Me(OH)_2$ precursors at pH values >11 , a Taylor reactor was used.⁹¹ NCM811 precursors are also synthesized on lab scale in a bottom flask as comparison. Calcination and electrode preparation are done as described in the experimental section. Interestingly, samples synthesized in a reactor (either the Taylor or the tank reactor) show a lower initial discharge capacity (Taylor reactor: 188 mAh g^{-1} , tank reactor: 186 mAh g^{-1}) if compared to NCM811 synthesized in the lab (193 mAh g^{-1} , Fig. C-2A). However, in the case of the reactor synthesis the capacity retention is 97% after 80 cycles and 92% for NCM811 synthesized in the lab. Moreover, the NCM811 samples synthesized in a reactor show a discharge capacity of $>120 \text{ mAh g}^{-1}$ at 2C after 40 cycles while it is 115 mAh g^{-1} in the case of the lab synthesis. It is also found in literature, that NCM811 which shows an initial capacity $>190 \text{ mAh g}^{-1}$ offers a capacity retention of $<95\%$ after 80 cycles, cathodes with lower initial capacities offer a capacity retention of $>95\%$ (see Table C-1) although individual exception might exist, and a determination of the value is difficult since the cycling procedures differ a lot. Consequently, all samples in the present study were synthesized using a continuous stirred tank reactor as described in the experimental section. The capacity retention of NCM111 and NCM622 after 80 cycles, which seems a better value to evaluate the cycling performance of layered oxides than the initial discharge capacity, is in both cases 97%.

Time-resolved *operando* synchrotron X-ray powder diffraction (SXPd, Beamline I11, DLS UK; PSD detector, $l = 0.489951(10) \text{ \AA}$) of the 1st and the 50th cycle is used to study the (long term) performance of the NCMs. Cycling was performed between 3.0 V and 4.3 V at a c-rate of C/5 using a 2 times overbalanced graphite

electrode (SGL) as counter electrode. The 1st and the 50th cycle were measured at 25 °C while the 2nd to the 49th cycle was performed at 45 °C outside the beamline hutch. Fig. C-3 shows the 003 reflections of NCM111, NCM622 and NCM811 upon the 1st (A) and the 50th cycle (B) and the corresponding crystallographic data (C-H) obtained from Rietveld refinement. The major difference between the 1st and the 50th cycle is an inactive phase present after 50 cycles, as marked in Fig. C-3B with dashed lines (splitting of the 003 reflection). The electrochemically inactive phase of NCM811 and NCM622 show lattice parameters in the order of the discharged, completely lithiated materials while in NCM111 a less active phase is present (the lattice parameters of both phases are changing significantly) between 75 mAh g^{-1} and 100 mAh g^{-1} (Figs. C-3D and C-3F) which indicates that the degradation of NCM111 is less severe. The phase content of the less active or inactive phases drops to zero before reaching the end of charge which means no capacity loss is found. Upon extensive cycling (> 1000 cycles) the content of the less active or inactive phase increases, leading to a point, where (partially) discharged material is left even at the end of charge which results in severe capacity losses.^{89,92–94} Whether these electrochemically less or inactive phases occur due to isolated particles (crack formation) and/or due to an incomplete delithiation of the NCM particles (resistance rise due to surface degradation and reconstruction) is still under discussion.

Upon the 1st cycle no reflections splitting is observed. Instead, smooth changes in microstrain (anisotropic predominantly in c direction) between 0 and 100 mAh g^{-1} and a rapid rise after 155 mAh g^{-1} is observed (Fig. C-3G). This correlates with the collapse in the c lattice parameter (Fig. C-3E) and the $O-O_{\text{tet}}$ distance discussed in the main text (Fig. C-3B). It is worth mentioning, that no increase in the Li/Me disorder was observed, not within the 1st nor from the 1st to the 50th cycle although the Li/Me disorder of $\sim 2.5\%$ is close to the detection limit.

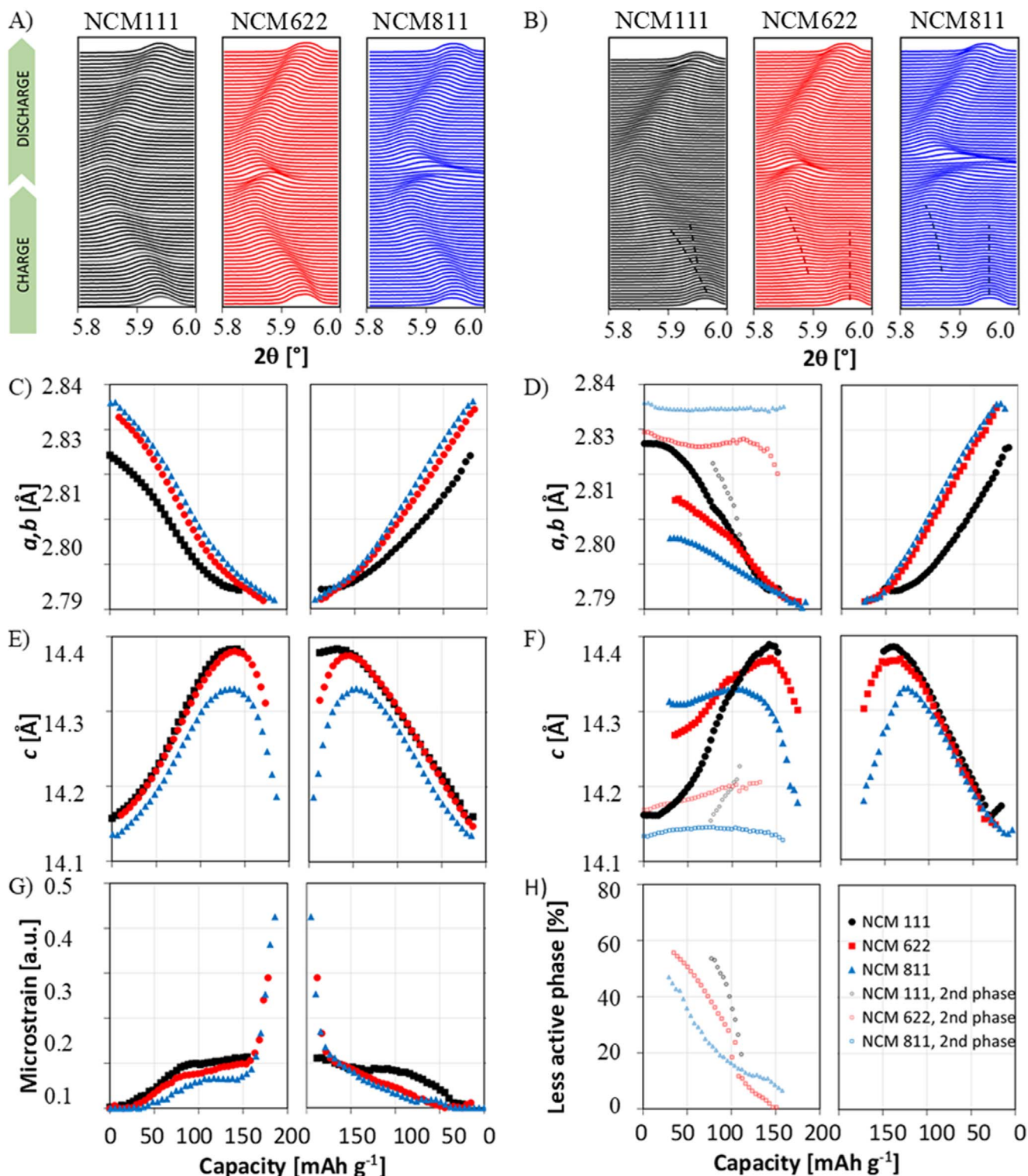


Figure C-3. Synchrotron powder diffraction data and analysis with (A), (B), the evolution of the 003 reflection, (C), (D) the a, b lattice parameter and (E), (F), the c lattice parameter evolution upon the 1st (A), (C) and (E) and the 50th cycle (B), (D) and (F) of NCM111, NCM622 and NCM811. (G) shows the evolution of microstrain upon the 1st cycle, (H) the percentage of the observed, inactive phase upon the 50th cycle (charge).

Appendix D. Choice of Reference Material

Ni in NCM111, NCM622 and NCM811 shows a mixed $\text{Ni}^{2+}/\text{Ni}^{3+} \approx \text{Ni}^{2+}$ low spin configuration as discussed in the main text, Fig. D-1. Table D-I lists the results of the Ni $L_{2,3}$ edge simulations of NCM111, NCM622 and NCM811 in the charged state, at a 1st discharge capacity of 150 mAh g⁻¹, 100 mAh g⁻¹, 50

mAh g⁻¹ and in the discharged state. The corresponding NEXAFS data is shown in Fig. D-1. The spectra are simulated using a superposition of a Ni^{2+} (96% $3d^8$ and 4% $3d^9$ L) and Ni^{3+} (20%–30% $3d^7$ and 70%–80% $3d^8$ L) as described in the main text.

The Co $L_{2,3}$ and Mn $L_{2,3}$ edge of charged and discharged NCM111, NCM622 and NCM811 are shown in Figs. D-2A and

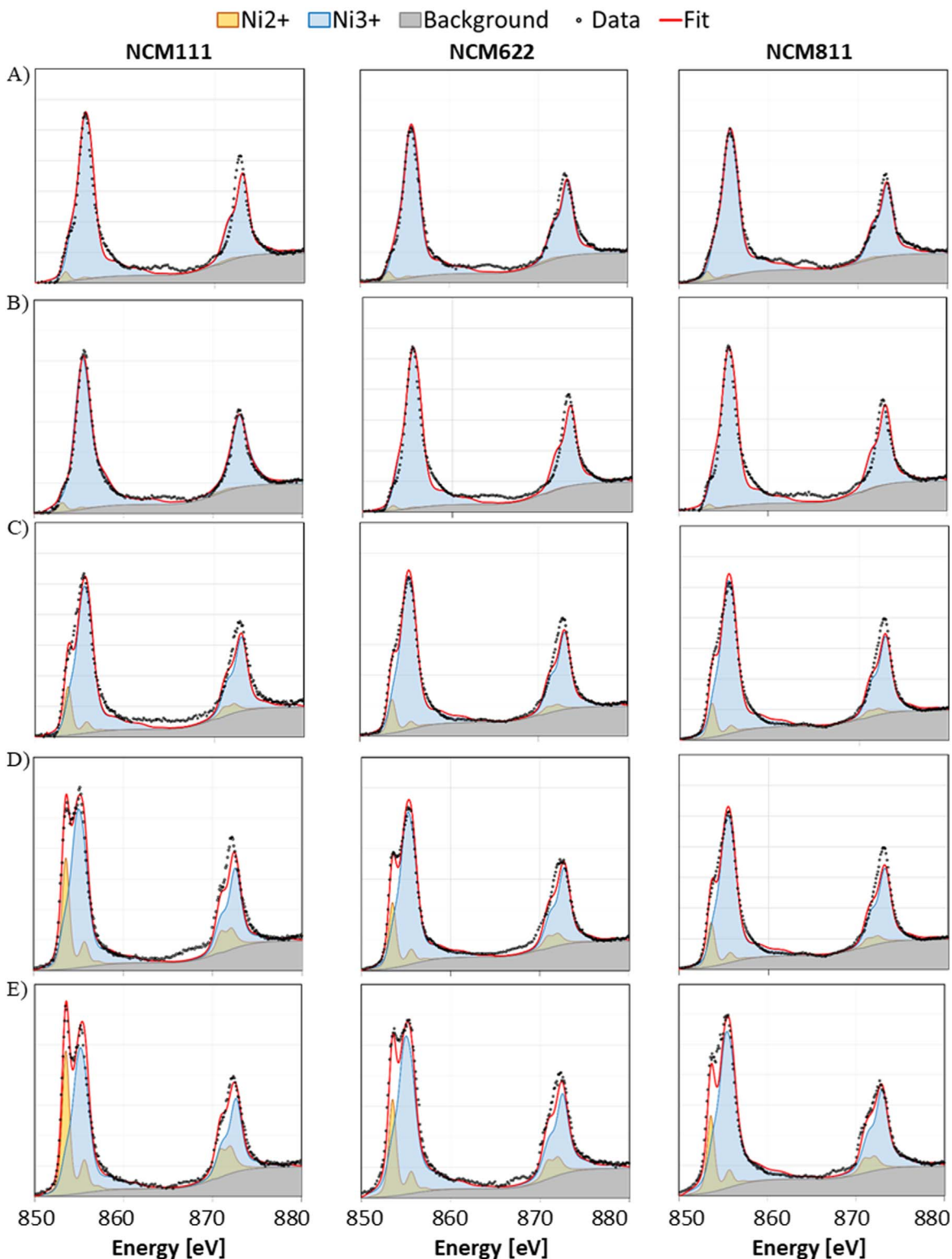


Figure D-1. Ni $L_{2,3}$ edge of NCM111, NCM622 and NCM811 charged to 4.3 V (A), at 150 mAh g^{-1} (B), 100 mAh g^{-1} (C), 50 mAh g^{-1} (D) and in the discharged state (E), simulated with charge-transfer multiplet calculations.

D-2B, respectively. Upon the first discharge no changes are observed showing that Co and Mn are not redox active in the bulk. The contrasts to literature are discussed in the main text.

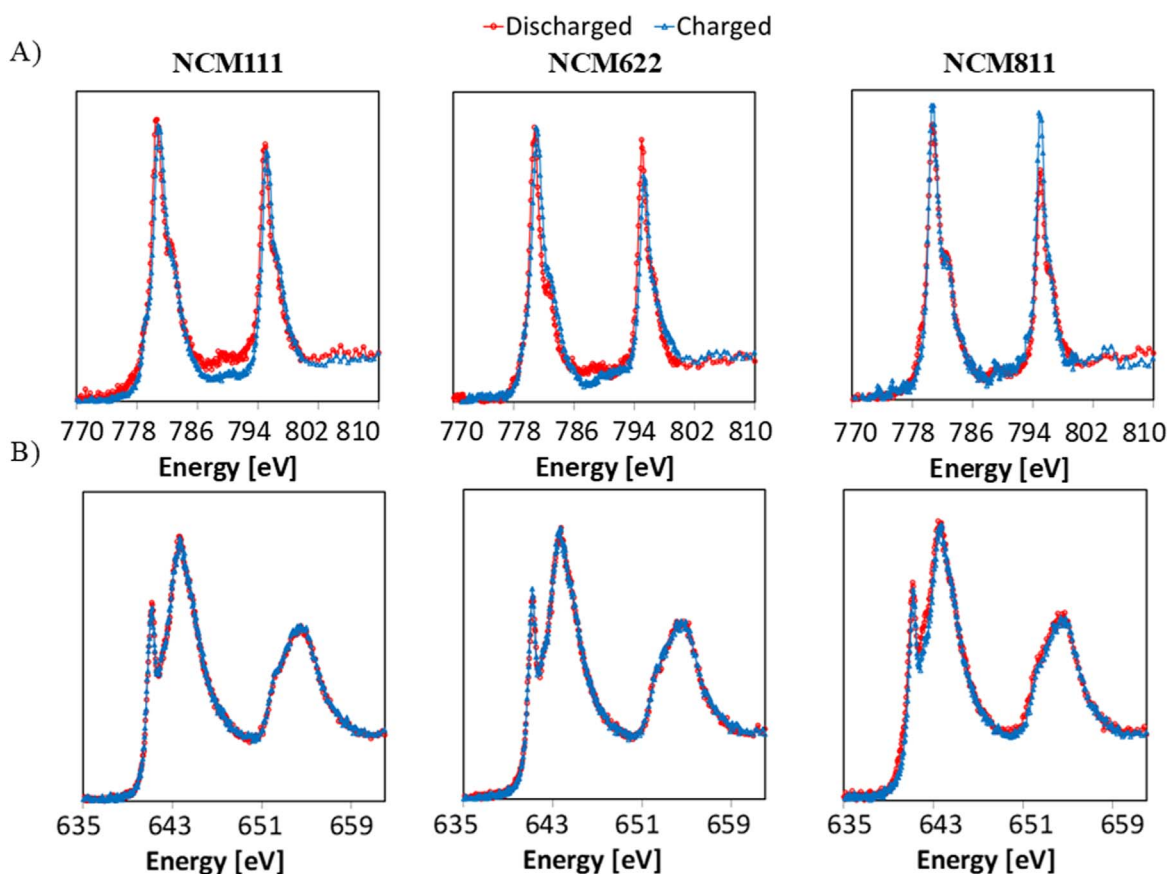
Fig. D-3A shows the measured data (NCM111, black dots) and the CTM calculation of Mn^{4+} (red line and blue filling), obtained by taking various, higher excited configurations such as $3d^{3+x}L^x$ with $0 \leq x \leq 2$ into account. The Co $L_{2,3}$ spectra (although noisier

compared to Ni) can be described with a Co^{3+} low spin configuration ($LF = 3.0 \text{ eV}$) as shown in Fig. D-3B. The CTM calculations describe the spectra sufficiently without ligand-to-metal charge-transfer (LMCT) from O to Co.

For the choice of the reference materials, the electronic configuration of the transition metals Me need to be the same as in the case of NCM111, NCM622 and NCM811. Moreover, the references

Table D-I. Ni, Ni²⁺, Ni³⁺, Co and Mn ratio in relation to the overall Me content in NCM111, NCM622 and NCM811.

Material	State of charge [mAh g ⁻¹]	Ni [Me-%]	Ni ²⁺ [Me-%]	Ni ³⁺ [Me-%]	Co/Mn [Me-%]
NCM111 Li _x Ni _{1/3} Co _{1/3} Mn _{1/3} O ₂	163	33	1	32	33
	150	33	1	32	33
	100	33	6	27	33
	50	33	11	22	33
	0	33	19	14	33
NCM622 Li _x Ni _{0.6} Co _{0.2} Mn _{0.2} O ₂	182	60	3	57	20
	150	60	1	59	20
	100	60	7	53	20
	50	60	14	46	20
	0	60	23	37	20
NCM811 Li _x Ni _{0.8} Co _{0.1} Mn _{0.1} O ₂	186	80	3	77	10
	150	80	1	79	10
	100	80	12	68	10
	50	80	16	64	10
	0	80	35	55	10

**Figure D-2.** Co $L_{2,3}$ (A) and Mn $L_{2,3}$ edge XAS spectra (B) of charged (blue) and discharged (red) NCM111, NCM622 and NCM811.

should be isostructural to (or at least should show a similar structure than) the rhombohedral $R\bar{3}m$ structure of the layered oxides. Therefore, rhombohedral LCO (LiCoO₂, Co³⁺ low spin) and LNO (LiNiO₂, Ni^{2+/3+} low spin) is used. Mn in LiMnO₂ has a $t_{2g}^4 e_g^0$ (formal Mn³⁺) configuration and is therefore not appropriate for a comparison to a $t_{2g}^3 e_g^0$ (formal Mn⁴⁺) configuration present in the NCMs. Instead, LLO (Li₂MnO₃ = Li(Li_{1/3}Mn_{2/3})O₂), which is structurally related to rhombohedral layered oxides,¹⁶ served as

reference. Fig. D-4 shows NEXAFS data and the refinement of the crystallographic structure of LNO, LCO and LLO. All discharged NEXAFS spectra look like the corresponding Ni $L_{2,3}$, Co $L_{2,3}$ and Mn $L_{2,3}$ edges of NCM111, NCM622 and NCM811. The charged Co $L_{2,3}$ and Mn $L_{2,3}$ spectra of LCO and LLO show slight changes if compared to the discharged ones. While in NCM neither Co nor Mn is electrochemically active, the transition metals show a certain redox activity if no Ni is present.

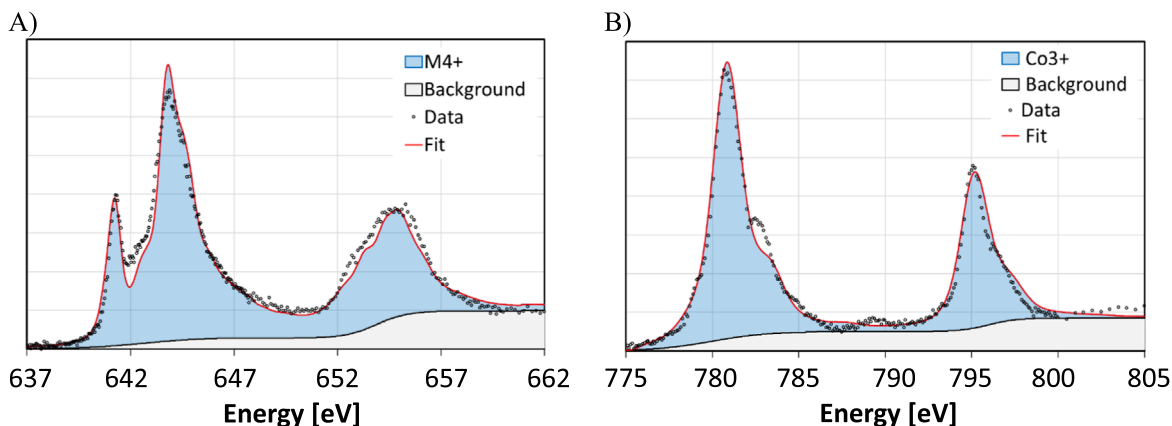


Figure D-3. (A) Mn $L_{2,3}$ spectra, calculated with Quanty. The Mn $L_{2,3}$ edge was simulated with a superposition of $3d^{3+x}\underline{L}^x$ configurations. (B) $3d^6$ configuration of Co, fitted with CTM4XAS.

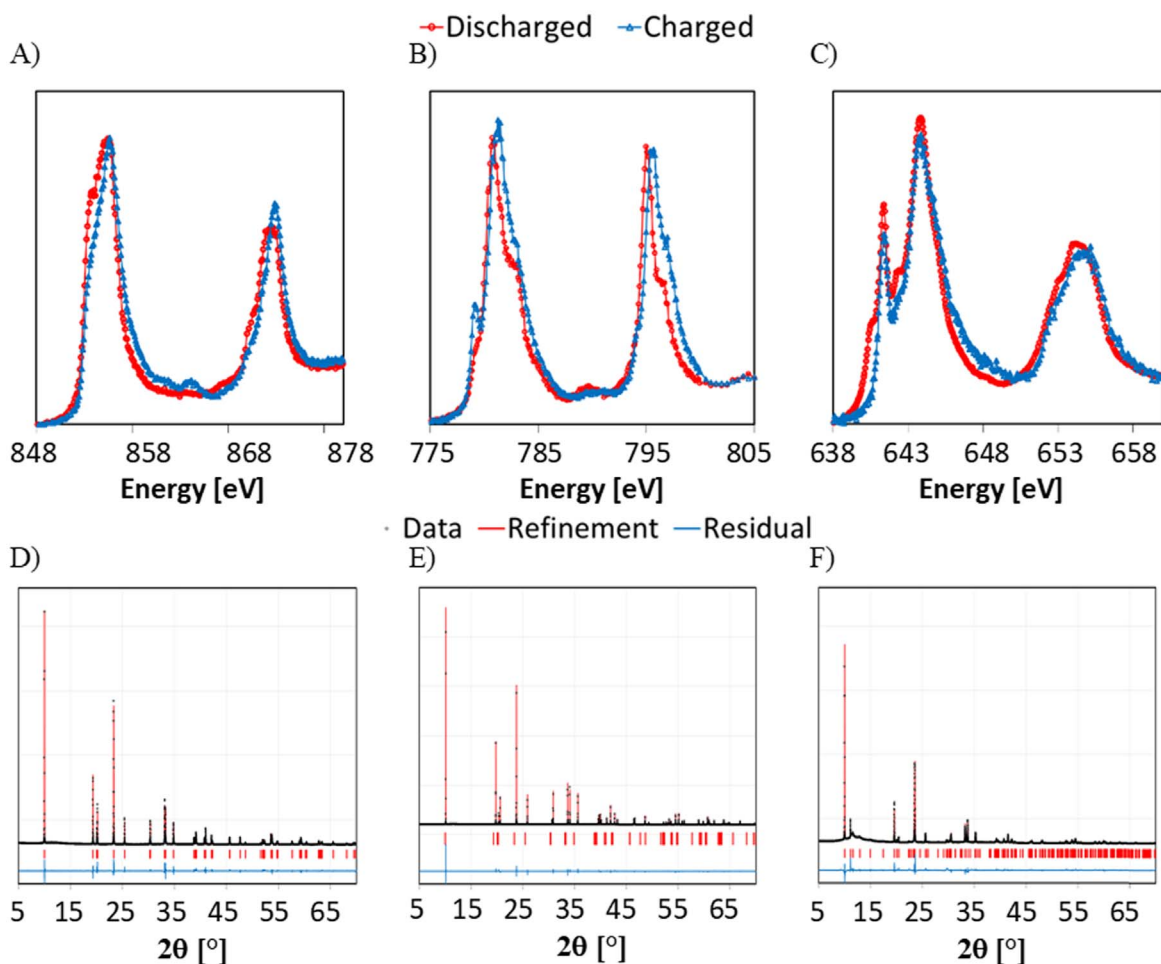


Figure D-4. (A) Ni $L_{2,3}$ edge of LNO, (B) Co $L_{2,3}$ edge of LCO and (C), Mn $L_{2,3}$ edge of LLO, measured in the charged (red) and in discharged state (blue). (D) and (E) shows the Rietveld refinement of LNO and LCO with the rhombohedral structure and (F), LLO with the monoclinic $C/2m$ structure.

Appendix E. Comparison of the Ni $L_{2,3}$ edge of the charged NCMs to Ni^{4+} simulations

In the following section the Ni $L_{2,3}$ edge of charged NCM111, NCM622 and NCM811 is compared to the charge transfer multiplet (CTM) calculations of Ni^{4+} shown in the main text, Fig. 2A. All spectra calculated with the configuration Ni $3d^{6+y}\underline{L}^y$ ($0 \leq y \leq 1$) are shown in Figs. E-1A–E-1D. \underline{L} denotes a hole at O 2p sites, the ligand-field energy was varied from 1 eV to 4 eV from the left to the

right, and the core hole potential U_{pd} and the on-site Coulomb interactions U_{dd} were kept constant ($U_{pd} - U_{dd} = 1$ eV).

The best match of the charged Ni $L_{2,3}$ NEXAFS spectra and the Ni^{4+} CTM calculations is obtained at ligand field energies ≥ 3 eV for $y = 0$. However, the energy difference between the main peaks of the L_3 and the L_2 edge of the measured and the calculated data differs significantly, as indicated in Figs. E-1C and E-1D with the vertical, dotted lines. Moreover, pronounced multiplet and satellite features

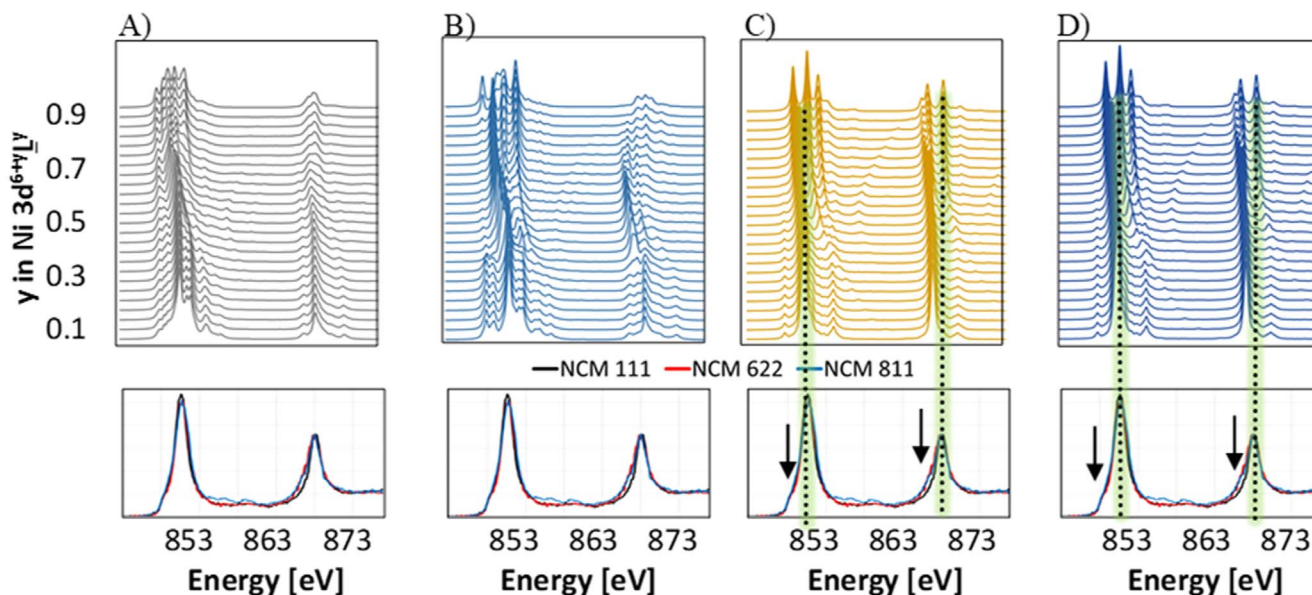


Figure E-1. Charge transfer multiplet calculations of Ni $3d^{6+y} L^y$ ($0 \leq y \leq 1$) with a ligand field energy of 1 eV (A), 2 eV (B), 3 eV (C) and 4 eV (D). The data is compared to the charged Ni L_{2,3} spectra of NCM111, NCM622 and NCM811 (panels below the waterfall plots of the CTM calculations).

~ 2 eV before and after the main peak of the L_3 edge and ~ 2 eV after the L_2 edge present in the calculations are missing in the measured NCM spectra. Moreover, low energetic shoulders observed for both edges (main peaks) in the measured spectra (marked with arrows in the NCM spectra, Fig. E-1, panels below the waterfall plots) are absent in the calculations.

Appendix F. Degradation Reactions Upon the 1st Cycle

The cathode electrolyte interphase (CEI) was analyzed using TEY NEXAFS spectroscopy which has a sampling depth of ~ 10 nm and was measured simultaneously with the FY spectra. In the O K spectra (Fig. F-1A), the decreasing Ni–O Hybrid peaks (528 eV–530 eV) and the increasing Ni²⁺ peaks (532 eV–535 eV) indicate that covalent Ni³⁺ reacts to more ionic Ni²⁺ as discussed for the bulk in the main text. The occurrence of Ni²⁺ peaks between 531 eV and 535 eV as well as their shift to lower energies upon extensive cycling due to the formation of NiO or NiO-like phases on the surface was discussed elsewhere.^{64,95} CEI products (peaks at e.g. 533 eV for LiNiPO₄ and 534 eV - 535 eV for Li₂CO₃,^{87,88}) are not visible if not obscured by Me–O peaks. The F K spectra show the presence of PvdF and/or LiF, Fig. F-1B⁹⁶ but the spectra do not reveal any change upon discharge. In innumerable publications it

was shown, that NCM111, NCM622 and NCM811 undergo irreversible reactions at capacities > 155 mAh g⁻¹ upon the 1st charge (Table F-I). References which discuss the onset of these reactions are marked with “*”. This agrees with the F K spectra of NCM811 measured upon the 1st cycle, Fig. F-1C: Changes in the F K edge are observed around 690 eV, where LiF is expected to have a shoulder.⁹⁶ The shoulder disappears above 155 mAh g⁻¹, which agrees with the onset of gas evolution,⁹⁷ the loss of Li salts⁹⁸ and surface reconstruction reactions^{76,99} listed in Table F-I. Whether the decreasing LiF shoulder is due to volumetric changes NCMs undergo at high potentials, transition metal dissolution with HF involved¹⁴ or other chemical reactions^{15,42,76,100} cannot be deduced from the present data. The degradation reactions upon the 1st charge (Table F-I) include gas formation, surface reconstruction reactions (NiO formation), transition metal dissolution and electrolyte decomposition reactions. The detrimental reactions are accompanied with a breakdown in diffusion kinetics and all these reactions alter the surfaces of the NCM particles, which has long-term effects on the performance of the cathodes (see Appendix C). Between 155 mAh g⁻¹ and the charged state of the NCMs Ni is slightly reduced as indicated by the increasing shoulder at 853 eV (Figs. F-1D–F-1F). At the same time, Ni–O hybrid peaks between 528 eV and 532 eV decrease in intensity (Figs. F-1G–F-1I).

Table F-I. Literature survey on degradation reactions of layered oxides upon the 1st cycle and after extensive cycling. References which discuss the onset of irreversible reactions are marked with “*”.**Gas formation**

*J. Electrochem. Soc. 163, A798 (2016).	NCM111 NCM622 NCM811	Onset of CO ₂ and CO evolution at ca. 155 mAh g ⁻¹ (1st charge) - CO ₂ : 4.1 V; CO: 4.0 V. Onset of O ₂ formation at 4.3 V.
* J. Phys. C. 121, 13481 (2017).		
* ACS Appl. Mater. Interfaces 10, 38892 (2018).		
J. Electrochem. Soc. 164 A1361 (2017).	NCM811	Variation of the cutoff voltage: O ₂ release at > 4.3 V cause capacity fade.
J. Electrochem. Soc. 166, A1853 (2019).		
* Mater. Today 21, 825 (2018).	NCM111 NCM811	Singlet oxygen: Onset at ~155 mAh g ⁻¹ .
Surface reconstructions/Crystallographic changes		
ACS Appl. Energy Mater. 3, 4799 (2020).	NCM111 NCM622 NMC811	Mechanism of surface reconstruction.
Adv. Energy Mater. 9, 1901597 (2019).		
Adv. Energy Mater. 7, 1602888 (2017).		
*Adv. Mater. 32, 2001741 (2020).	NCM111 NCM622 NCM811	Strong correlation between CO ₂ /O ₂ release and surface reconstruction.
*Electrochem. Solid-State Lett. 5, A2 (2002).	NCM622	CO ₂ formation: Reaction of electrolyte and NCM.
* J. Phys. Chem. C 121, 3286 (2017).	NCM111 NCM811	Anisotropic micro-strain rises at ~155 mAh g ⁻¹ .
Transition metal dissolution		
Power Sources 329, 364 (2016).	NCM111 NCM523 NCA	Me dissolution is enhanced with higher cutoff voltages (4.3 V—4.6 V) and with an increasing number of cycles.
J. Electrochem. Soc. 164 A389 (2017).		
* J. Mater. Chem. A 4, 18300 (2016).		
* J. Phys. Chem. A 122, 8828 (2018)		
* Mater. Today 21, 825 (2018).	NCM111 NCM811	Me caused by singlet oxygen - correlation with the onset of gas evolution.
Breakdown in diffusion kinetics		
*J. Mater. Chem. A 8, 8540 (2020).	NCM811	Breakdown of kinetics upon the 1st cycle at. ~155 mAh g ⁻¹ .
* Chem. Mater. 31, 2545 (2019).		
*J. Am. Chem. Soc. 140, 6767 (2018).	NCM622	Polarization rise at ~155 mAh g ⁻¹
Electrolyte decomposition		
*Chem.Mater.2018, 30, 958.	NCM811 NCA	Electrolyte decomposition (formation of LiF, Li ₂ CO ₃ , Li _x PO _y F _y , NiO) occurs mainly at elevated temperatures. Loss of Li-impurities (LiF, Li ₂ CO ₃) on the surface starts at ~4.0 V.
ACS Sustainable Chem. Eng. 8, 7316 (2020).		
Adv. Mater. 32, 2001741 (2020).		
Electrochem.Solid-State Lett. 5, A2 (2002).		

Table F-I. (Continued).**Formation of inactive or less active material/Crack formation/Impedance rise**

ACS Appl. Energy Mater. 2, 7375 (2019).	NCM811 NCM	Charge transfer resistance increase upon long-term cycling along with crack formations & surface morphology changes.
J. Phys. Chem. C 121, 26163 (2017).	851005	
J. Electrochem. Soc. 166, A3760 (2019).		
ACS Appl. Energy Mater. 3, 2821 (2020).	NCM 851005	Formation of inactive or less active phases.

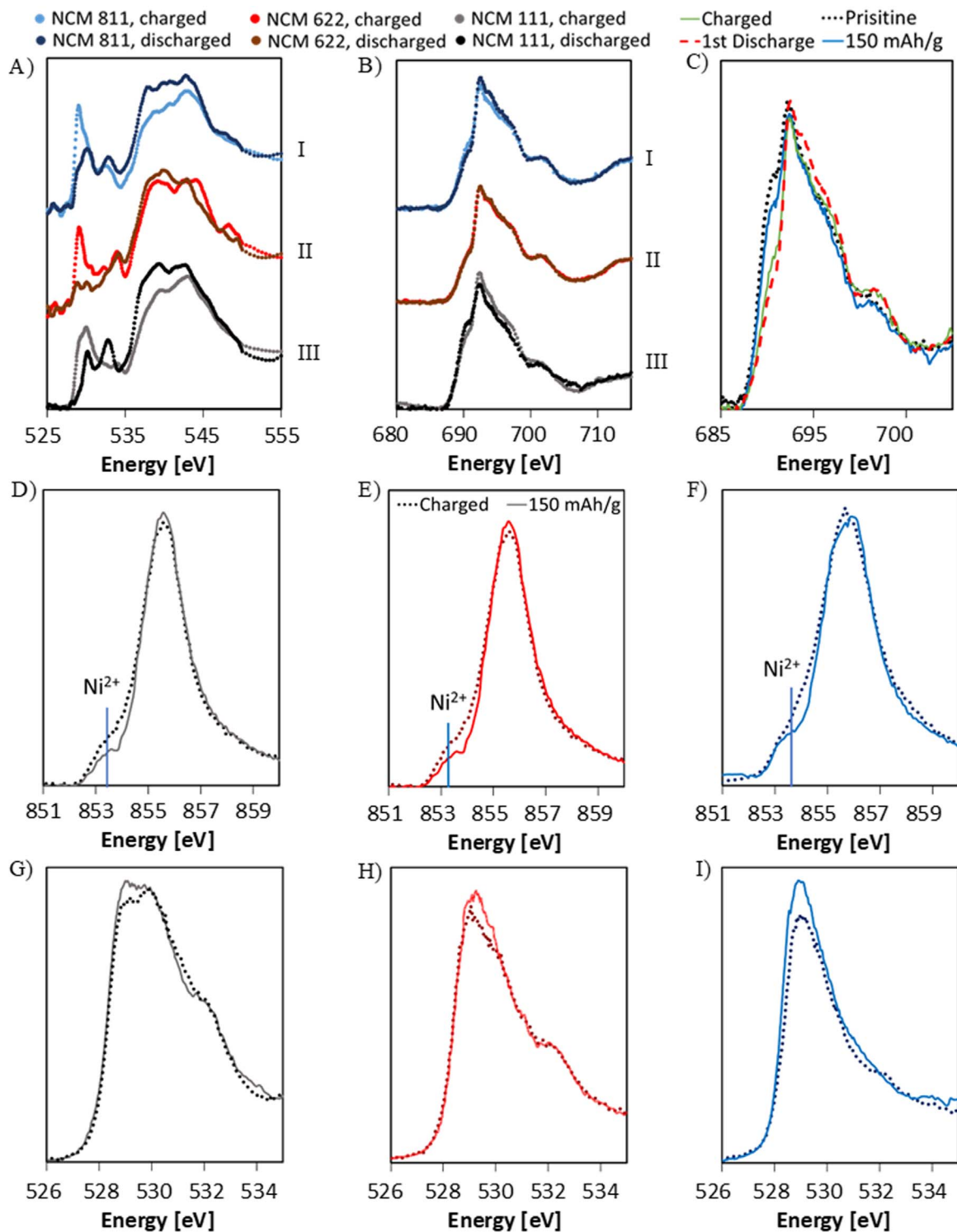


Figure F-1. Total electron yield (TEY) O K (A) and F K spectra (B) of charged and discharged NCM811 (I), NCM622 (II) and NCM111 (III). (C) TEY F K edge of pristine NCM811 (dotted line), NCM811 after 150 mAh g⁻¹ charge (blue solid line), NCM811 in the charged state (green solid line) and after the 1st cycle in the discharged state (dashed line). (D)–(I) depict the Ni L₃ (D)–(F) and O K spectra (G)–(I) of NCM111, NCM622 and NCM811 (solid lines: charged NCMs; dotted lines: samples discharged to 150 mAh g⁻¹ upon the 1st cycle).

Appendix G. Kinetic Limitations

The influence of kinetic issues on the presented data (e.g., voltage, capacity) is evaluated using the galvanostatic intermittent titration technique (GITT, Fig. G-1A). NCM111, NCM622 and NCM811 are charged and discharged in 3-electrode Swagelok cells using 41 × 30 min C/20 current pulses followed by a 10 h rest (or a

rest until the voltage drop becomes < 0.001 V/20 s) to reach conditions close to equilibrium. At the end of charge the cells are charged to 4.3 V with C/20 and hold at this voltage for 5 h. Please note that for the GITT measurements higher initial charge capacities are achieved if compared to the C/20 cycle (NCM811: 227 mAh g⁻¹, NCM622: 192 mAh g⁻¹, NCM111: 167 mAh g⁻¹). While upon

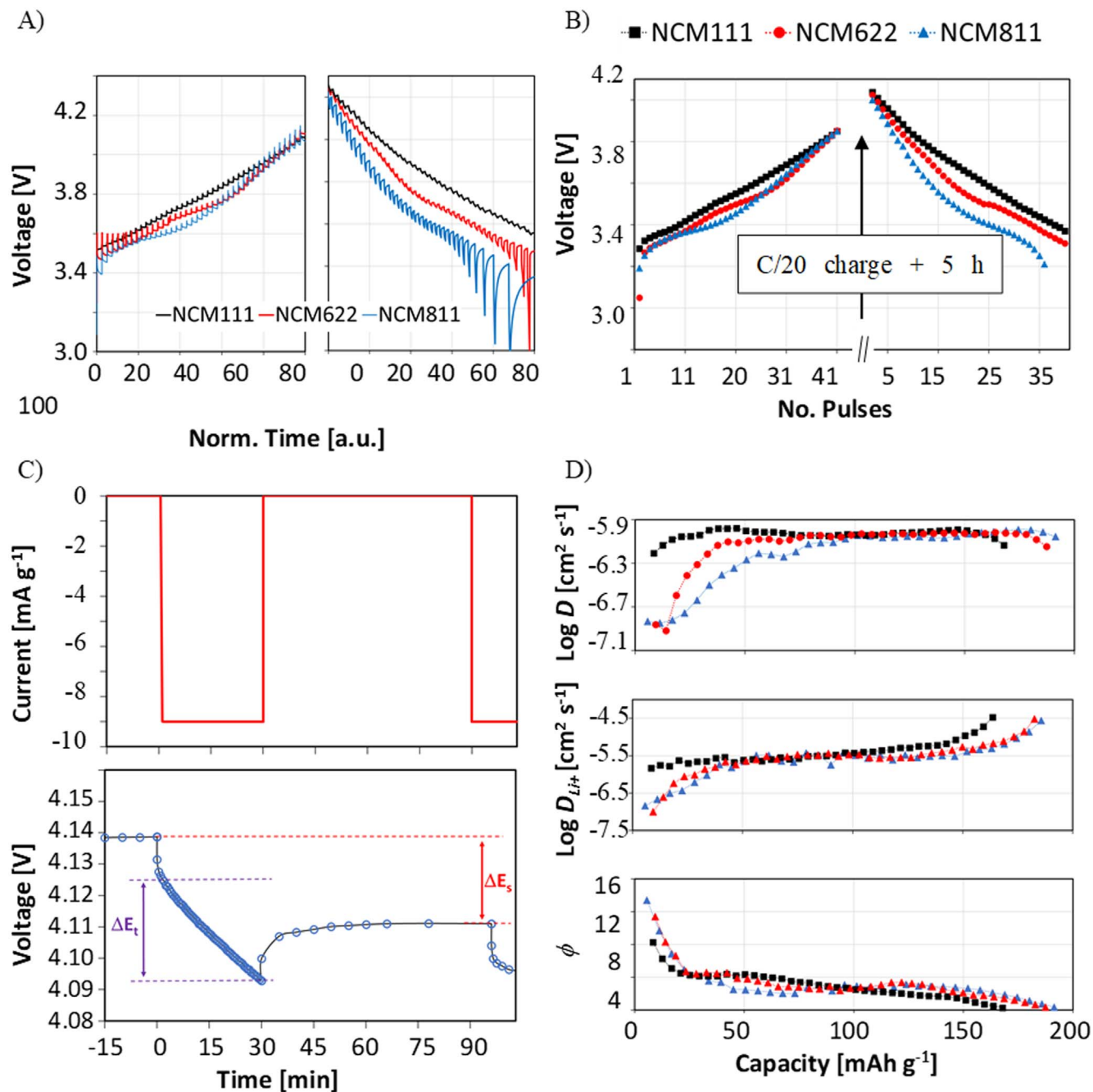


Figure G-1. Galvanostatic intermittent titration technique (GITT) measurements of NCM111, NCM622 and NCM811 (A) with the equilibrium voltage curve (B) and a depiction of a GITT pulse (C). ΔE_s is the difference in the steady state potential of two consecutive pulses while ΔE_t (which is a function of the square root of time) is the magnitude of the voltage change (minus the IR drop). (D) gives the determined logarithmic diffusion coefficient $\text{Log } D$, the thermodynamic factor ϕ and the logarithmic Li diffusion coefficient $\text{Log } D_{Li^+}$.

charge all materials underwent 41 current pulses until they reached the cutoff voltage, the number of current pulses performed upon discharge in the case of NCM811 is by two lower than that of NCM622 and NCM111 due to the lower, initial efficiency (NCM811: 90.3%, NCM622: 96.7%, 96.8%). Fig. G-1B shows the steady state potential E_s (explanation see Fig. G-1C) obtained at the end of each rest step upon the GITT-discharge of the NCMs. The mean discharge voltage of NCM111 is 3.85 V, for NCM622 it is 3.79 V and of NCM811 it is 3.75 V, respectively. To further explore kinetic limitations and to correlate the findings to crystallographic and spectroscopic observations, the discharge pulses were analyzed to determine the chemical diffusions coefficients D , the


thermodynamic factor ϕ and the Li-mobility D_{Li^+} (Fig. G-1D).⁶⁴ The chemical diffusion coefficient D can be derived using Fick's 1st law, it is a function of $(\Delta E_s / E_t)^2$, it is the product of a thermodynamic factor ϕ (thermodynamic driving force, function of $\Delta E_s / \partial x$ with x , the Li content in Li_xMeO_2) and the Li-ion mobility D_{Li^+} ($D = D_{Li^+} \cdot \phi$) and it describes the reaction kinetics of the rate limiting step.

Differences in diffusion kinetics of NCM111, NCM622 and NCM811 are predominantly observed at low states of charge ($< 75 \text{ mAh g}^{-1}$) where the Li-content x in Li_xMeO_2 is close to one and almost no Li vacancies are present, Fig. G-1D (1st panel). Thus, no Li hopping from the inside to the outside of the particles can take

place (the Li mobility D_{Li^+} is relatively low, Fig. G-1D, middle panel) and charge exchange reactions through the cathode electrolyte interphase (CEI) are the rate limiting processes.^{64,101} Differences in the surface area, as deduced in Appendix B are probably the origin of differences in kinetics at low states of charge: NCM111 has with 0.39 m²/g the highest BET area and thus charge exchange reactions through the interface are faster. The BET area of NCM622 (0.34 m² g⁻¹) and NCM 811 (0.36 m² g⁻¹), both values are remarkably close, show a lower BET area compared to NCM111. Consequently, charge exchange reactions proceed slower since less redox active sites (and mobile Li ions) are present on the surface and the diffusion coefficients D (Li diffusion coefficients D_{Li^+}) are lower. With an increasing state of charge, D and D_{Li^+} increase due to the formation of Li-vacancies in the bulk material, which enables Li-hopping. However, the thermodynamic driving force (the lithium gradient depicted by ϕ , Fig. G-1D, bottom panel) decreases relatively quickly until it reaches an almost constant value because the surface near regions of the particles become Li-depleted. The chemical diffusion coefficient D increases through a minimum and reaches a plateau at ~ 50 mAh g⁻¹ (x in Li_xMeO₂ > 0.1). At ~ 155 mAh g⁻¹ (x in Li_xMeO₂ < 0.56) the number of mobile charge carriers in the bulk material becomes limiting,^{64,101} resulting in a breakdown of diffusion kinetics for all materials. This is the point where the crystallographic structure (the O–O_{tet} distances) collapses, see main text Fig. 3B.

ORCID

Karin Kleiner  <https://orcid.org/0000-0003-0203-440X>

Michael Merz  <https://orcid.org/0000-0002-7346-7176>

References

- H. Förster, S. Gores, C. Nissen, A. Siemons, N. Renders, S. Dael, M. Sporer, and M. Tomescu, *National Action Across All Sectors Needed to Reach Greenhouse Gas Effort Sharing targets*, European Environment Agency Luxembourg (2020).
- L. Hockstad, S. Burke, A. Bunkerdirected, M. Desai, M. Weitz, C. Hight, R. Schmeltz, T. Wirth, D. Ottinger, and D. Godwin et al., *U.S. Greenhouse Gas Emissions and Sinks: 1990-2014* (2016) 11–733 United States Environmental Protection Agency Washington .
- B. Scrosati and J. Garche, "Lithium Batteries: Status, Prospects and Future." *J. Power Sources* , **195**, 2419 (2010).
- M. Winter, B. Barnett, and K. Xu, "Before Li Ion Batteries." *Chem. Rev.*, **118**, 11433 (2018).
- W. Bernhart, "Lithium-Ion Batteries—New Business Models Emerging." AABC, Virtual(Roland Berger Strategy Consultants GmbH Sr Partner) (2020) .
- L. Goldie-Scott, "Electric Vehicles: The End of the Beginning." AABC, Virtual (Bloomberg New Energy Finance, Head of Clean Power) (2020).
- D. Andre, S.-J. Kim, P. Lamp, S. F. Lux, F. Maglia, O. Paschos, and B. Stiaszny, "Future generations of cathode materials: an automotive industry perspective." *J. Mater. Chem. A* , **3**, 6709 (2015).
- R. Schmich, R. Wagner, G. Höppl, T. Placke, and M. Winter, "Performance and cost of materials for lithium-based rechargeable automotive batteries." *Nat. Energy* , **3**, 267 (2018).
- S.-T. Myung, F. Maglia, K.-J. Park, C. S. Yoon, P. Lamp, S.-J. Kim, and Y.-K. Sun, "Nickel-rich layered cathode materials for automotive lithium-ion batteries: achievements and perspectives." *ACS Energy Lett.* , **2**, 196 (2017).
- M. M. Thackeray, C. Wolverton, and E. D. Isaacs, "Electrical energy storage for transportation—approaching the limits of, and going beyond, lithium-ion batteries." *Energy Environ. Sci.* , **5**, 7854 (2012).
- O. Guillon et al., *Advanced Ceramics for Energy Conversion and Storage* (Elsevier, Jülich) (2020), (<https://linkinghub.elsevier.com/retrieve/pii/S20170040788>).
- O. Gröger, H. A. Gasteiger, and J.-P. Suchsland, "Review—electromobility: batteries or fuel cells ?" *J. Electrochem. Soc.* , **162**, A2605 (2015).
- M. D. Radin, S. Hy, M. Sina, C. Fang, H. Liu, J. Vinkeviciute, M. Zhang, M. S. Whittingham, Y. S. Meng, and A. Van der Ven, "Narrowing the gap between theoretical and practical capacities in Li-Ion layered oxide cathode materials." *Adv. Energy Mater.* , **7**, 1602888 (2017).
- K. Kleiner and H. Ehrenberg, "Challenges considering the degradation of cell components in commercial lithium-ion cells: a review and evaluation of present systems." *Top. Curr. Chem.* , **375**, 45 (2017).
- R. Jung, M. Metzger, F. Maglia, C. Stinner, and H. A. Gasteiger, "Oxygen release and its effect on the cycling stability of LiNi x Mn y Co z O₂ (NMC) cathode materials for li-ion batteries." *J. Electrochem. Soc.* , **164**, A1361 (2017).
- K. Kleiner, B. Strehle, A. R. Baker, S. J. Day, C. C. Tang, I. Buchberger, F.-F. Chesneau, H. A. Gasteiger, and M. Piana, "Origin of high capacity and poor cycling stability of li-rich layered oxides: a long-duration in situ synchrotron powder diffraction study." *Chem. Mater.* , **30**, 3656 (2018).
- O. Dolotko, a Senyshyn, M. J. Mühlbauer, K. Nikolowski, and H. Ehrenberg, "Understanding structural changes in NMC Li-ion cells by in situ neutron diffraction." *J. Power Sources* , **255**, 197 (2014).
- A. O. Kondrakov, A. Schmidt, J. Xu, H. Geßwein, R. Mönig, P. Hartmann, H. Sommer, T. Brezesinski, and J. Janek, "Anisotropic lattice strain and mechanical degradation of high- and low-nickel NCM cathode materials for Li-Ion batteries." *J. Phys. Chem. C* , **121**, 3286 (2017).
- J. N. Reimers and J. R. Dahn, "Electrochemical and In Situ X-ray diffraction studies of lithium intercalation in LiXCoO₂." *J. Electroanal. Chem.* , **139**, 2 (1992).
- L. De Biasi, B. Schwarz, T. Brezesinski, P. Hartmann, J. Janek, and H. Ehrenberg, "Chemical, structural, and electronic aspects of formation and degradation behavior on different length scales of Ni-Rich NCM and Li-Rich HE-NCM cathode materials in Li-Ion batteries." *Adv. Mater.* , **31**, 1900985 (2019).
- L. De Biasi, A. O. Kondrakov, H. Geßwein, T. Brezesinski, P. Hartmann, and J. Janek, "Between scylla and charybdis: balancing among structural stability and energy density of layered NCM cathode materials for advanced lithium-ion batteries." *J. Phys. Chem. C* , **121**, 26163 (2017).
- C. Xu et al., "Bulk fatigue induced by surface reconstruction in layered Ni-rich oxide cathodes for Li-ion batteries." *Nature Materials* , **20**, 84-92 (2021).
- W. S. Yoon et al., "In situ soft XAS study on nickel-based layered cathode material at elevated temperatures: a novel approach to study thermal stability." *Sci. Rep.* , **4**, 6827 (2014).
- W.-S. Yoon, K. Y. Chung, J. McBreen, D. A. Fischer, and X.-Q. Yang, "Electronic structural changes of the electrochemically Li-ion deintercalated LiNi_{0.8}Co_{0.15}Al_{0.05}O₂ cathode material investigated by X-ray absorption spectroscopy." *J. Power Sources* , **174**, 1015 (2007).
- L. A. Montoro, M. Abbate, and J. M. Rosolen, "Electronic structure of transition metal ions in deintercalated and reintercalated LiCo_{0.5}Ni_{0.5}O₂." *J. Electrochem. Soc.* , **147**, 1651 (2000).
- L. A. Montoro, M. Abbate, E. C. Almeida, and J. M. Rosolen, "Electronic structure of the transition metal ions in LiCoO₂, LiNiO₂ and LiCo_{0.5}Ni_{0.5}O₂." *Chem. Phys. Lett.* , **309**, 14 (1999).
- C. Tian, D. Nordlund, H. L. Xin, Y. Xu, Y. Liu, D. Sokaras, F. Lin, and M. M. Doeff, "Depth-Dependent Redox Behavior of LiNi_{0.6} Mn_{0.2} Co_{0.2} O₂." *J. Electrochem. Soc.* , **165**, A696 (2018).
- W. S. Yoon, M. Balasubramanian, K. Y. Chung, X. Q. Yang, J. McBreen, C. P. Grey, and D. A. Fischer, "Investigation of the charge compensation mechanism on the electrochemically Li-ion deintercalated Li_{1-x}Co_{1/3}Ni_{1/3}Mn_{1/3}O₂ electrode system by combination of soft and hard X-ray absorption spectroscopy." *J. Am. Chem. Soc.* , **127**, 17479 (2005).
- M. G. Kim, N. E. Sung, H. J. Shin, N. S. Shin, K. S. Ryu, and C. H. Yo, "Ni and oxygen K-edge XAS investigation into the chemical bonding for lithiation of Li_yNi_{1-x}Al_xO₂ cathode material." *Electrochim. Acta* , **50**, 501 (2004).
- F. de Groot and A. Kotani, *Core Level Spectroscopy of Solids* (CRC Press, Boca Raton) 6 (2008).
- M. W. Haverkort, M. Zwierzycki, and O. K. Andersen, "Multiplet ligand-field theory using Wannier orbitals." *Phys. Rev. B - Condens. Matter Mater. Phys.* , **85**, 165113 (2012).
- E. Stavitski and F. M. F. de Groot, "The CTM4XAS program for EELS and XAS spectral shape analysis of transition metal L edges." *Micron* , **41**, 687 (2010).
- Y. Lu, M. Höppner, O. Gunnarsson, and M. W. Haverkort, "Efficient real-frequency solver for dynamical mean-field theory." *Phys. Rev. B - Condens. Matter Mater. Phys.* , **90**, 60 (2014).
- F. de Groot, "High-resolution X-ray emission and X-ray absorption spectroscopy." *Chem. Rev.* , **101**, 1779 (2001).
- J. Lüder, J. Schött, B. Brena, M. W. Haverkort, P. Thunström, O. Eriksson, B. Sanyal, I. Di Marco, and Y. O. Kvashnin, "Theory of L-edge spectroscopy of strongly correlated systems." *Phys. Rev. B* , **96**, 245131 (2017).
- Z. Hu, M. Golden, J. Fink, G. Kaindl, S. Warda, D. Reinen, P. Mahadevan, and D. Sarma, "Hole distribution between the Ni 3d and O 2p orbitals in Nd_{2-x}Sr_xNiO_{4-δ}." *Phys. Rev. B* , **61**, 3739 (2000).
- J. M. Tarascon, G. Vaughan, Y. Chabre, L. Seguin, M. Anne, P. Strobel, and G. Amatucci, "In situ structural and electrochemical study of Ni_{1-x}CoxO₂ metastable oxides prepared by soft chemistry." *J. Solid State Chem.* , **147**, 410 (1999).
- M. Saubanère, E. McCalla, J.-M. Tarascon, M.-L. Doublet, M. Saubanère, E. McCalla, J.-M. Tarascon, and M.-L. Doublet, "The intriguing question of anionic redox in high-energy density cathodes for Li-ion batteries." *Energy Environ. Sci.* , **9**, 984 (2016).
- G. Assat, D. Foix, C. Delacourt, A. Iadecola, R. Dedryvère, and J.-M. Tarascon, "Fundamental interplay between anionic/cationic redox governing the kinetics and thermodynamics of lithium-rich cathodes." *Nat. Commun.* , **8**, 2219 (2017).
- G. Assat and J.-M. Tarascon, "Fundamental understanding and practical challenges of anionic redox activity in Li-ion batteries." *Nat. Energy* , **3**, 373 (2018).
- M. Sathiyaraj et al., "Reversible anionic redox chemistry in high-capacity layered-oxide electrodes." *Nat. Mater.* , **12**, 827 (2013).
- K. Luo et al., "Charge-compensation in 3d-transition-metal-oxide intercalation cathodes through the generation of localized electron holes on oxygen." *Nat. Chem.* , **8**, 684 (2016).
- R. A. House et al., "Superstructure control of first-cycle voltage hysteresis in oxygen-redox cathodes." *Nature* , **577**, 502 (2020).
- E. McCalla et al., "Visualization of O-O peroxo-like dimers in high-capacity layered oxides for Li-ion batteries." *Science (80-.)* , **350**, 1516 (2015).
- M. Merz, B. Ying, P. Nagel, S. Schuppeler, and K. Kleiner, "Reversible and irreversible redox processes in Li-rich layered oxides." *Chemistry of Materials* , **In Press** (2021).

46. Z. W. Lebens-Higgins et al., "Revisiting the charge compensation mechanisms in LiNi_{0.8}Co_{0.2-y}Al_yO₂ systems." *Mater. Horizons*, **6**, 2112 (2019).
47. G.-H. Lee, J. W. Wu, D. Kim, K. Cho, M. Cho, W. Yang, and Y.-M. K. Kang, "Reversible anionic redox activities in conventional LiNi_{1/3}Co_{1/3}Mn_{1/3}O₂ Cathodes." *Angew. Chem. Int. Ed.*, **59**, 2 (2020).
48. A. O. Kondrakov et al., "Charge-transfer-induced lattice collapse in Ni-Rich NCM cathode materials during delithiation." *J. Phys. Chem. C*, **121**, 24381 (2017).
49. A. Manthiram and J. B. Goodenough, "Lithium insertion into Fe₂(SO₄)₃ frameworks." *J. Power Sources*, **26**, 403 (1989).
50. C. Liu, Z. G. Neale, and G. Cao, "Understanding electrochemical potentials of cathode materials in rechargeable batteries." *Mater. Today*, **19**, 109 (2016).
51. M. S. Wu, P. C. J. Chiang, J. C. Lin, and Y. S. Jan, "Correlation between electrochemical characteristics and thermal stability of advanced lithium-ion batteries in abuse tests - Short-circuit tests." *Electrochim. Acta*, **49**, 1803 (2004).
52. H.-J. Noh, S. Youn, C. S. Yoon, and Y. Sun, "Comparison of the structural and electrochemical properties of layered Li[Ni_xCo_yMn_z]O₂ (x = 1/3, 0.5, 0.6, 0.7, 0.8 and 0.85) cathode material for lithium-ion batteries." *J. Power Sources*, **233**, 121 (2014).
53. M. Lee, Y. Kang, S. Myung, and Y. Sun, "Synthetic optimization of Li[Ni_{1/3}Co_{1/3}Mn_{1/3}]O₂ via co-precipitation." *Electrochim. Acta*, **50**, 939 (2004).
54. C. J. Han, J. H. Yoon, W. Il Cho, and H. Jang, "Electrochemical properties of LiNi_{0.8}Co_{0.2-x}Al_xO₂ prepared by a sol-gel method." *J. Power Sources*, **136**, 132 (2004).
55. A. J. Achkar, T. Z. Regier, H. Wadati, Y.-J. Kim, H. Zhang, and D. G. Hawthorn, "Bulk sensitive X-ray absorption spectroscopy free of self-absorption effects." *Phys. Rev. B*, **83**, 081106 (2011).
56. M. Merz, P. Nagel, C. Pinta, A. Samartsev, H. V. Löhneysen, M. Wissinger, S. Uebe, A. Assmann, D. Fuchs, and S. Schuppler, "X-ray absorption and magnetic circular dichroism of LaCoO₃, La_{0.7}Co_{0.3}CoO₃, and La_{0.7}Sr_{0.3}CoO₃ films: evidence for cobalt-valence-dependent magnetism." *Phys. Rev. B*, **82**, 174416 (2010).
57. M. Merz, D. Fuchs, A. Assmann, S. Uebe, H. V. Löhneysen, P. Nagel, and S. Schuppler, "Spin and orbital states in single-layered La_{2-x}CaxCoO₄ studied by doping- and temperature-dependent near-edge X-ray absorption fine structure." *Phys. Rev. B*, **84**, 014436 (2011).
58. S. P. Thompson, J. E. Parker, J. Marchal, J. Potter, A. Birt, F. Yuan, R. D. Fearn, A. R. Lennie, S. R. Street, and C. C. Tang, "Fast X-ray powder diffraction on 111 at diamond." *J. Synchrotron Radiat.*, **18**, 637 (2011).
59. J. Rodriguez-Carvajal and T. Roisnel, *FullProf.98 and WinPLOTR: New Windows 95/NT Applications for Diffraction; in Extended software/methods development issue Newsletter N°20*, International Union of Crystallography (1998)35-36.
60. S.-C. Yin, Y.-H. Rho, I. Swainson, and L. F. Nazar, "X-ray/neutron diffraction and electrochemical studies of lithium De/Re-Intercalation in Li_{1-x}Co_{1/3}Ni_{1/3}Mn_{1/3}O₂ (x = 0 → 1)." *Chem. Mater.*, **18**, 1901 (2006).
61. X. Zheng, X. Li, Z. Huang, B. Zhang, Z. Wang, H. Guo, and Z. Yang, "Enhanced electrochemical performance of LiNi_{0.6}Co_{0.2}Mn_{0.2}O₂ cathode materials by ultrasonic-assisted co-precipitation method." *J. Alloys Compd.*, **644**, 607 (2015).
62. H. Arai, M. Tsuda, and Y. Sakurai, "Lithium nickelate electrodes with enhanced high-temperature performance and thermal stability." *J. Power Sources*, **90**, 76 (2000).
63. G. Cherkashinin, M. Motzko, N. Schulz, T. Späth, and W. Jaegermann, "Electron spectroscopy study of Li[Ni_{0.8}Co_{0.15}Al_{0.05}]O₂ electrolyte interface: electronic structure, interface composition, and device implications." *Chem. Mater.*, **27**, 2875 (2015).
64. K. Kleiner, J. Melke, M. Merz, P. Jakes, P. Nagel, S. Schuppler, V. Liebau, and H. Ehrenberg, "Unraveling the degradation process of LiNi_{0.8}Co_{0.15}Al_{0.05}O₂ electrodes in commercial lithium ion batteries by electronic structure investigations." *ACS Appl. Mater. Interfaces*, **7**, 19589 (2015).
65. Y.-N. Zhou et al., "High-rate charging induced intermediate phases and structural changes of layer-structured cathode for lithium-ion batteries." *Adv. Energy Mater.*, **6**, 1600597 (2016).
66. X. Zeng, C. Zhan, J. Lu, and K. Amine, "Stabilization of a high-capacity and high-power nickel-based cathode for Li-Ion." *Batteries Chem.*, **4**, 690 (2018).
67. M. Oishi et al., "Charge compensation mechanisms in Li_{1.16}Ni_{0.15}Co_{0.19}Mn_{0.50}O₂ positive electrode material for Li-ion batteries analyzed by a combination of hard and soft X-ray absorption near edge structure." *J. Power Sources*, **222**, 45 (2013).
68. C. Liang, W. Zhang, Z. Wei, Z. Wang, Q. Wang, and J. Sun, "Transition-metal redox evolution and its effect on thermal stability of LiNi_{1-x}Co_xMn_{1-x-y}O₂ based on synchrotron soft X-ray absorption spectroscopy." *J. Energy Chem.*, **59**, 446 (2021).
69. R. J. Green, M. W. Haverkort, and G. A. Sawatzky, "Bond disproportionation and dynamical charge fluctuations in the perovskite rare-earth nickelates." *Phys. Rev. B*, **94**, 195127 (2016).
70. V. I. Anisimov, J. Zaanen, and O. K. Andersen, "Band theory and mott insulators: hubbard U instead of stoner I." *Phys. Rev. B*, **44**, 943 (1991).
71. M. Saubanere, E. McCalla, J.-M. Tarascon, and M.-L. Doublet, "The intriguing question of anionic redox in high-energy density cathodes for Li-ion batteries." *Energy Environ. Sci.*, **9**, 984 (2016).
72. A. Van der Ven and G. Ceder, "Lithium diffusion mechanisms in layered intercalation compounds." *J. Power Sources*, **97-98**, 529 (2001).
73. K. Märker, P. J. Reeves, C. Xu, K. J. Griffith, and C. P. Grey, "Evolution of structure and lithium dynamics in LiNi_{0.8}Mn_{0.1}Co_{0.1}O₂ (NMC811) cathodes during electrochemical cycling." *Chem. Mater.*, **31**, 2545 (2019).
74. W. Li, H. Y. Asl, Q. Xie, and A. Manthiram, "Collapse of LiNi_{1-x-y}Co_xMn_yO₂ lattice at deep charge irrespective of nickel content in lithium-ion batteries." *J. Am. Chem. Soc.*, **141**, 5097 (2019).
75. C. Hong, Q. Leng, J. Zhu, S. Zheng, H. He, Y. Li, R. Liu, J. Wan, and Y. Yang, "Revealing the correlation between structural evolution and Li⁺ diffusion kinetics of nickel-rich cathode materials in Li-ion batteries." *J. Mater. Chem. A*, **8**, 8540 (2020).
76. D. Streich, C. Erk, A. Guéguen, P. Müller, F.-F. Chesneau, and E. J. Berg, "Operando monitoring of early ni-mediated surface reconstruction in layered Lithiated Ni-Co-Mn oxides." *J. Phys. Chem. C*, **121**, 13481 (2017).
77. T. Hatsukade, A. Schiele, P. Hartmann, T. Brezesinski, and J. Janek, "Origin of carbon dioxide evolved during cycling of nickel-rich layered NCM cathodes." *ACS Appl. Mater. Interfaces*, **10**, 38892 (2018).
78. M. Evertz, F. Horsthemke, J. Kasnatscheew, M. Börner, M. Winter, and S. Nowak, "Unraveling transition metal dissolution of Li_{1.04}Ni_{1/3}Co_{1/3}Mn_{1/3}O₂ (NCM 111) in lithium ion full cells by using the total reflection X-ray fluorescence technique." *J. Power Sources*, **329**, 364 (2016).
79. B. Michalak, B. B. Berkes, H. Sommer, T. Bergfeldt, T. Brezesinski, and J. Janek, "Gas Evolution in LiNi_{0.5}Mn_{1.5}O₄/graphite cells studied in operando by a combination of differential electrochemical mass spectrometry, neutron imaging, and pressure measurements." *Anal. Chem.*, **88**, 2877 (2016).
80. B. Strehle, K. Kleiner, R. Jung, F. Chesneau, M. Mendez, H. A. Gasteiger, and M. Piana, "The role of oxygen release from Li- and Mn-Rich layered oxides during the first cycles investigated by on-line electrochemical mass spectrometry." *J. Electrochem. Soc.*, **164**, A400 (2017).
81. M. Eilers-Rethwisch, S. Hildebrand, M. Evertz, L. Ibing, T. Dagger, M. Winter, and F. M. Schappacher, "Comparative study of Sn-doped Li[Ni_{0.6}Mn_{0.2}Co_{0.2-x}Sn_x]O₂ cathode active materials (x = 0-0.5) for lithium ion batteries regarding electrochemical performance and structural stability." *J. Power Sources*, **397**, 68 (2018).
82. S. Gao, B. Shi, J. Liu, L. Wang, C. Zhou, C. Guo, J. Zhang, and W. Li, "Boron doping and LiBO₂ coating synergistically enhance the high-rate performance of LiNi_{0.6}Co_{0.1}Mn_{0.3}O₂ cathode materials." *ACS Sustain. Chem. Eng.*, **9**, 5322 (2021).
83. F. Zhou, X. Zhao, and J. R. Dahn, "Synthesis, electrochemical properties, and thermal stability of Al-Doped LiNi_{1/3}[sub 1/3]Mn_{1/3}[sub 1/3-z]Co_z[sub z]O₂ Positive Electrode Materials." *J. Electrochem. Soc.*, **156**, A343 (2009).
84. C. Janiak, H.-J. Meyer, D. Gudat, and P. Kurz, *Riedel Moderne Anorganische Chemie* (De Gruyter, Boston, Berlin) (2018).
85. P. Atkins and J. de Paula, *Physical Chemistry* (Oxford University Press, New York, NY) 9 ed. (2010).
86. K. Edström, T. Gustafsson, and J. O. Thomas, "The cathode-electrolyte interface in the Li-ion battery." *Electrochim. Acta*, **50**, 397 (2004).
87. S. Yang, D. Wang, G. Liang, Y. M. Yiu, J. Wang, L. Liu, X. Sun, and T.-K. Sham, "Soft X-ray XANES studies of various phases related to LiFePO₄ based cathode materials." *Energy Environ. Sci.*, **5**, 7007 (2012).
88. R. Qiao, Y. Chuang, S. Yan, and W. Yang, "Soft X-ray irradiation effects of Li₂O₂, Li₂CO₃ and Li₂O revealed by absorption spectroscopy." *PLoS One.*, **7**, 3 (2012).
89. K. Kleiner, D. Dixon, P. Jakes, J. Melke, Y. Murat, C. Roth, K. Nikolowski, V. Liebau, and H. Ehrenberg, "Fatigue of LiNi_{0.8}Co_{0.15}Al_{0.05}O₂ in commercial Li ion batteries." *J. Power Sources*, **273**, 70 (2015).
90. S. P. Thompson, J. E. Parker, J. Potter, T. P. Hill, A. Birt, T. M. Cobb, F. Yuan, and C. C. Tang, "Beamline 111 at diamond: a new instrument for high resolution powder diffraction." *Rev. Sci. Instrum.*, **80**, 1 (2009).
91. M. Seenivasan, C.-C. Yang, S. Wu, W.-C. Chien, Y.-S. Wu, R. Jose, and S. J. Lue, "Using a Couette-Taylor vortex flow reactor to prepare a uniform and highly stable Li[Ni_{0.8}Co_{0.15}Al_{0.05}]O₂ cathode material." *J. Alloys Compd.*, **857**, 157594 (2021).
92. S. Schweidler, L. de Biasi, G. Garcia, A. Mazilkin, P. Hartmann, T. Brezesinski, and J. Janek, "Investigation into mechanical degradation and fatigue of high-Ni NCM cathode material: a long-term cycling study of full cells." *ACS Appl. Energy Mater.*, **2**, 7375 (2019).
93. S. Schweidler, L. de Biasi, P. Hartmann, T. Brezesinski, and J. Janek, "Kinetic limitations in cycled nickel-rich NCM Cathodes and Their Effect on the Phase Transformation Behavior." *ACS Appl. Energy Mater.*, **3**, 2821 (2020).
94. M. S. D. Darma, M. Lang, K. Kleiner, L. Mereacre, V. Liebau, F. Fauth, T. Bergfeldt, and H. Ehrenberg, "The influence of cycling temperature and cycling rate on the phase specific degradation of a positive electrode in lithium ion batteries: a post mortem analysis." *J. Power Sources*, **327**, 714 (2016).
95. M. Balasubramanian, H. S. Lee, X. Sun, X. Q. Yang, A. R. Moodenbaugh, J. McBreen, D. A. Fischer, and Z. Fu, "Formation of SEI on cycled lithium-ion battery cathodes: soft X-ray absorption study." *Electrochem. Solid-State Lett.*, **5**, A22 (2002).
96. Y. Joly, C. Cavallari, S. A. Guda, and C. J. Sahle, "Full-Potential Simulation of X-ray Raman Scattering Spectroscopy." *J. Chem. Theory Comput.*, **13**, 2172 (2017).
97. M. Metzger, B. Strehle, S. Solchenbach, and H. A. Gasteiger, "Origin of H₂ evolution in LIBs: H₂O Reduction vs electrolyte oxidation." *J. Electrochem. Soc.*, **163**, A798 (2016).
98. Z. W. Lebens-Higgins et al., "Evolution of the electrode-electrolyte interface of LiNi_{0.8}Co_{0.15}Al_{0.05}O₂ electrodes due to electrochemical and thermal stress." *Chem. Mater.*, **30**, 958 (2018).
99. J. Zhu, S. Sharifi-Asl, J. C. Garcia, H. H. Iddir, J. R. Croy, R. Shahbazian-Yassar, and G. Chen, "Atomic-level understanding of surface reconstruction based on Li [Ni_xMn_yCo_{1-x-y}]O₂ Single-Crystal Studies." *ACS Appl. Energy Mater.*, **3**, 4799 (2020).
100. A. Guéguen, D. Streich, M. He, M. Mendez, F. F. Chesneau, P. Novák, and E. J. Berg, "Decomposition of LiPF₆ in high energy lithium-ion batteries studied with online electrochemical mass spectrometry." *J. Electrochem. Soc.*, **163**, A1095 (2016).
101. L. A. Montoro and J. M. Rosolen, "The role of structural and electronic alterations on the lithium diffusion in Li_xCo_{0.5}Ni_{0.5}O₂." *Electrochim. Acta*, **49**, 3243 (2004).